WATER RESOURCES RESEARCH, VOL. 49, 5134–5154, doi:10.1002/wrcr.20373, 2013

Modeling erosion and sedimentation coupled with hydrological and overland flow processes at the watershed scale

Jongho Kim,[1] Valeriy Y. Ivanov,[1] and Nikolaos D. Katopodes[1]

Received 1 October 2012; revised 14 June 2013; accepted 17 June 2013; published 4 September 2013.

[1] A novel two-dimensional, physically based model of soil erosion and sediment transport coupled to models of hydrological and overland flow processes has been developed. The Hairsine-Rose formulation of erosion and deposition processes is used to account for size-selective sediment transport and differentiate bed material into original and deposited soil layers. The formulation is integrated within the framework of the hydrologic and hydrodynamic model tRIBS-OFM, Triangulated irregular network-based, Real-time Integrated Basin Simulator-Overland Flow Model. The integrated model explicitly couples the hydrodynamic formulation with the advection-dominated transport equations for sediment of multiple particle sizes. To solve the system of equations including both the Saint-Venant and the Hairsine-Rose equations, the finite volume method is employed based on Roe's approximate Riemann solver on an unstructured grid. The formulation yields space-time dynamics of flow, erosion, and sediment transport at fine scale. The integrated model has been successfully verified with analytical solutions and empirical data for two benchmark cases. Sensitivity tests to grid resolution and the number of used particle sizes have been carried out. The model has been validated at the catchment scale for the Lucky Hills watershed located in southeastern Arizona, USA, using 10 events for which catchment-scale streamflow and sediment yield data were available. Since the model is based on physical laws and explicitly uses multiple types of watershed information, satisfactory results were obtained. The spatial output has been analyzed and the driving role of topography in erosion processes has been discussed. It is expected that the integrated formulation of the model has the promise to reduce uncertainties associated with typical parameterizations of flow and erosion processes. A potential for more credible modeling of earth-surface processes is thus anticipated.

Citation: Kim, J., V. Y. Ivanov, and N. D. Katopodes (2013), Modeling erosion and sedimentation coupled with hydrological and overland flow processes at the watershed scale, *Water Resour. Res.*, *49*, 5134–5154, doi:10.1002/wrcr.20373.

1. Introduction

[2] Soil erosion and excessive sedimentation are among the most important threats to sustainable agriculture and watershed management worldwide [*Oldeman et al.*, 1991; *Bai et al.*, 2008]. Erosion leads to significant soil loss [*Buringh*, 1981; *Brown*, 1984] and imposes substantial social costs [*Pimentel et al.*, 1995; *Noel*, 2001]. Major problems and concerns related to soil erosion are as follows. (1) Rainfall- and runoff-induced erosion from watersheds and farm fields produce major nonpoint source pollutants for many significant environmental resources [*Hogarth et al.*, 2004b]. (2) River bank erosion and the associated rise of channel bed can lead to a diminished flow capacity and higher vulnerability to floods. (3) Land degradation caused by acceleration of agricultural activities, deforestation, and urbanization remove fertile topsoil, resulting in a decrease of agricultural productivity [*Fiener et al.*, 2008]. (4) Streamflow characteristics and erosion processes are critical in determining stream physical habitat properties and can be responsible for undesired ecological impacts on biotic composition [*Poff and Allan*, 1995; *Bunn and Arthington*, 2002; *Poff and Zimmerman*, 2010].

[3] In order to enhance the understanding of the erosion mechanism and investigate how to reduce social costs, a number of continuing efforts have been undertaken to simulate the erosion process over the last few decades. Depending on what model is given an emphasis in an overall approach, studies can be conceptually divided into two classes. First, hydrologically based erosion models can be categorized either as empirical or mechanistic. Empirical models are usually derived by processing data observed at a plot scale with further application of statistical or stochastic scaling techniques that extract general characteristics for parsimonious estimation of soil erosion. These models

Additional supporting information may be found in the online version of this article.

[1]Department of Civil and Environmental Engineering, University of Michigan, Ann Arbor, Michigan, USA.

Corresponding author: J. Kim, Department of Civil and Environmental Engineering, University of Michigan, Ann Arbor, MI 48103, USA. (kjongho@umich.edu)

©2013. American Geophysical Union. All Rights Reserved.
0043-1397/13/10.1002/wrcr.20373

Table 1. Hydraulics Based Erosion and Sediment Transport Models[a]

Study	Hydrology	Governing Equations	Method	Size Selectivity	Mesh
Cao et al. [2004]		1-D	FVM	Single	
Nord and Esteves [2005]	Green-Ampt	2-D	FDM	Single	Rectangular
Simpson and Castelltort [2006]		2-D	FVM	Single	Rectangular
Murillo et al. [2008]		2-D	FVM	Single	Triangular
Heng et al. [2009]		1-D	FVM	Multi	
Papanicolaou et al. [2010]		1-D	FVM	Multi	
This work	tRIBS	2-D	FVM	Multi	Triangular

[a]FVM denotes Finite Volume Method; FDM denotes Finite Difference Method.

have been widely used due to their simplicity and reduced computational cost and data requirements. However, empirical models are limited in their capabilities: they use lumped parameters that cannot be directly measured in the field and ignore nonlinearities, thus limiting transferability of parameters from one watershed to another. Conversely, mechanistic, or sometimes referred to as "physically based," models originate from conservation laws with parameters that bear distinct physical meaning. These models enforce mass conservation and simplified versions of momentum conservation for flow, as well as mass conservation for sediment that is present in both the flow and stream bed. For a detailed review of the most commonly used hydrologically based erosion models, the reader is referred to *Merritt et al*. [2003] and *Aksoy and Kavvas* [2005].

[4] As another type of approach to erosion and sediment transport modeling, hydraulics-based erosion models focus on accurate solutions of flow mechanisms and coupling sediment motions to the flow dynamics. These models generally do not consider hydrological processes, assuming artificial or "known" boundary conditions. They solve various simplified forms of the Saint-Venant or shallow-water equations combined with advection-dominated sediment transport equations. Among this type of models that have been recently developed are those reported in *Cao et al*. [2004], *Nord and Esteves* [2005], *Simpson and Castelltort* [2006], *Murillo et al*. [2008], *Heng et al*. [2009], and *Papanicolaou et al*. [2010]. All these studies represent modeling of flow and sediment processes in a spatially distributed (one- or two-dimensional) manner for a continuous, unsteady flow with the possibility of including multiple, consecutive rainfall events. They can calculate sediment concentrations and bed morphological changes as well as flow variables such as depth and velocity. Table 1 summarizes the essential features of these models.

[5] The performance of the aforementioned erosion models may vary depending on whether the models can credibly take into account predominant factors controlling soil erosion. Soil erosion is strongly affected by many external factors, such as meteorological forcing, subsurface water pore pressure, flow conditions, vegetation cover and land use, topography, and human activities. It is also influenced by the soil's inherent properties such as erodibility, cohesiveness, and particle size distribution. Among the external factors, meteorological forcing, land use, and topographic data are typically given as input to an erosion model, and the last two are usually known at sufficiently high accuracy. Given appropriate meteorological input, the performance of a model depends mainly on the capability to reproduce the remaining factors: hydrological dynamics, including subsurface and above-surface phenomena, and hydrodynamic flow motions caused by complex topography at the watershed scale. Similarly, while soil erodibility and cohesiveness are considered in many erosion models as parameters, sediment particle size distribution is not generally included and a single sediment size is used. Overall, among external and internal factors, hydrological and hydraulic characteristics and particle size distribution are arguably the three most crucial elements in modeling erosion because of several reasons: (1) the partition of rainfall into runoff and "losses" (e.g., infiltration) strongly influences the overall magnitude of sediment erosion; for example, the sensitivity to this partition is very high in semiarid areas, where more than 90% of precipitation can be lost to infiltration [*Nearing et al*., 2007]; (2) the two-dimensional spatial variability of hydraulic or sediment state variables due to precipitation, topography or man-made infrastructure can affect the capability of accurate prediction of detachment and deposition of sediment; and (3) size differences of bed material impact the load and spatiotemporal variability of sediment dynamics. From a practical point, it is particularly valuable to discern fine sediments because many materials that impair water quality tend to adhere to them.

[6] None of the advanced hydraulics-based erosion studies listed in Table 1 consider all of the crucial factors and thus satisfy the aforementioned needs. Specifically, some of these studies employ the one-dimensional formulations of governing equations for flow and sediment; only a few studies consider grain-size dependences. Moreover, most of these studies (with the exception of the study by *Nord and Esteves* [2005] that uses a simple the Green-Ampt method for estimating runoff-loss partition) take little account of hydrologic processes at a relevant level of detail. Capturing the proper runoff generation mechanisms such as saturation-excess runoff, perched and groundwater exfiltration as well as infiltration-excess runoff is however vital because runoff types and their production rates vary greatly depending on topography, climate, soil type, groundwater table, and initial conditions as well [*Noto et al*., 2008]. This work represents a first attempt to combine all necessary processes within a single framework.

[7] Previously developed hydrologic and hydrodynamic models are coupled here with the Hairsine-Rose (H-R) formulation [*Hairsine and Rose*, 1991, 1992; *Sander et al*., 2007] to describe soil erosion and sediment transport. The H-R model can account for size-selective sediment transport based on particle size distribution. The formulation differentiates the bed composition into original and deposited soil layers, recognizing whether material has an "intact" or a "loose" condition. Formulations of the governing equations and a description of the numerical model

Table 2. A Summary of Processes Considered in the Hydrologic Model tRIBS

Processes	Governing Equations and Methods
Rainfall interception	Rutter canopy water balance model [*Rutter et al*., 1971, 1975]
Surface energy balance	The combination equation method for latent heat flux [*Penman*, 1948; *Monteith*, 1965], gradient method for sensible heat flux [*Entekhabi*, 2000], and force-restore method for ground water flux [*Lin*, 1980; *Hu and Islam*, 1995]
Evapotranspiration	The bare soil evaporation [*Deardorff*, 1978], canopy evaporation, and transpiration [*Eltahir and Bras*, 1993]
Infiltration	Gravity-dominated unsaturated flow [*Cabral et al*., 1992; *Ivanov et al*., 2004b]
Groundwater dynamics	Quasi-3D Boussinesq's equation under the Dupuit-Forchheimer assumptions [*Ivanov et al*., 2004b]
Runoff generation	Saturation excess [*Dunne and Black*, 1970], infiltration excess [*Horton*, 1933], perched stormflow [*Weyman*, 1970], and groundwater exfiltration [*Hursh and Brater*, 1941]
Snowpack dynamics	Snowpack dynamic model [*Rinehart et al*., 2008]

are provided in sections 2 and 3. Model verification is subsequently carried out, in which simulation results are compared with analytical solutions and empirical data. Two benchmark laboratory cases dealing with rainfall-induced erosion and overland flow-induced erosion are used. Two sensitivity tests to a grid resolution and the number of particle sizes are carried out for a case study Lucky Hills watershed located in southeastern Arizona, USA. Model confirmation is carried out using observed data for 10 rainfall events with parameter values obtained through calibration for a single rainfall event. An analysis of the basin response when spatially distributed watershed descriptors of soil conductivity and surface roughness are included concludes this manuscript.

2. Governing Equations

[8] The present numerical model is composed of three primary components: hydrology (tRIBS: triangulated irregular network-based Real-time Integrated Basin Simulator), flow dynamics (OFM: Overland Flow Model), and erosion and sediment transport (H-R model). Governing equations or methods for the description of hydrologic processes considered in tRIBS are summarized in Table 2; for more detailed information, the reader is referred to *Ivanov et al*. [2004b]. The Overland Flow Model was developed by *Bradford and Katopodes* [1999] for simulating turbid underflows and was later extended to an unstructured triangular mesh [*Begnudelli and Sanders*, 2006]. It has been successfully used for a wide range of hydrodynamic applications of surface irrigation [*Bradford and Katopodes*, 2001], dam-break floods [*Begnudelli and Sanders*, 2007; *Begnudelli et al*., 2008] or urban floods [*Sanders et al*., 2008]; its computational efficiency was enhanced through a Local Time Stepping scheme [*Sanders*, 2008]. Most details of unstructured mesh formulation such as neighboring mapping functions follow the approach of *Begnudelli and Sanders* [2006].

[9] For the purpose of attaining a numerical solution in the erosion and sediment transport problem, the two-dimensional (2-D) Saint-Venant equations [*Leendertse*, 1967; *Liggett*, 1968; *Abbott*, 1974] coupled with a formulation of sediment mass conservation and bed morphology evolution are used. The 2-D Saint-Venant equations are based on the assumption of hydrostatic pressure distribution in the vertical, so they are appropriate for vertically mixed water bodies. These equations, based on a vertical coordinate system, not one aligned with the flow, in the conservative form are as follows

$$\frac{\partial h}{\partial t}+\frac{\partial (uh)}{\partial x}+\frac{\partial (vh)}{\partial y}=S_r, \tag{1}$$

$$\frac{\partial (uh)}{\partial t}+\frac{\partial \left(u^2h+\frac{gh^2}{2}\right)}{\partial x}+\frac{\partial (uvh)}{\partial y}=-gh\frac{\partial z_b}{\partial x}-C_D u\sqrt{u^2+v^2}, \tag{2}$$

$$\frac{\partial (vh)}{\partial t}+\frac{\partial (uvh)}{\partial x}+\frac{\partial \left(v^2h+\frac{gh^2}{2}\right)}{\partial y}=-gh\frac{\partial z_b}{\partial y}-C_D v\sqrt{u^2+v^2}, \tag{3}$$

where x, y, and t represent the Cartesian space and time; h is the flow depth; u and v are x and y directional depth-averaged velocities, respectively; g is the acceleration constant due to gravity; z_b is the bed elevation; C_D is the bed drag coefficient, which is parameterized by using Manning's coefficient, n, as $C_D = gn^2h^{-1/3}$; S_r is the net runoff production rate, which can also be negative (e.g., in order to represent an infiltrating surface). Four different types of runoff can be calculated by considering local hydrological processes of saturated-unsaturated flow [*Ivanov et al*., 2004b]; the runoff rate is used as the source term in the mass conservation equation. In equations (2) and (3), the first momentum source term represents gravity and the second term represents bottom friction.

[10] The unsteady, two-dimensional equations of the Hairsine-Rose (H-R) model [*Hairsine and Rose*, 1991, 1992; *Sander et al*., 2007] for particle size class i are given by a mass conservation equation for suspended sediment and a bed evolution equation for the deposited layer. The H-R model was compared with experimental data and found to be able to satisfactorily represent erosion processes [*Proffitt et al*., 1991; *Beuselinck et al*., 1998; *Huang et al*., 1999; *Heng et al*., 2011]. The 2-D H-R equations are

$$\frac{\partial (hc_i)}{\partial t}+\frac{\partial (uhc_i)}{\partial x}+\frac{\partial (vhc_i)}{\partial y}=e_i+e_{ri}+r_i+r_{ri}-d, \quad i=1,2,\cdots I \tag{4}$$

$$\frac{\partial M_i}{\partial t}=d_i-e_{ri}-r_{ri}, \quad i=1,2,\cdots I \tag{5}$$

$$(1-\beta)\rho_s\frac{\partial z_b}{\partial t}=\sum_{i=1}^{I}(d_i-e_i-e_{ri}-r_i-r_{ri}), \tag{6}$$

where c_i is the sediment concentration given as mass per unit volume $\left[\mathrm{M/L^3}\right]$; M_i is the sediment mass of the

deposited layer formulated as mass per unit area $[\mathrm{M/L^2}]$; I is the number of sediment size classes; and e_i, e_{ri}, r_i, r_{ri}, and d_i respectively denote rainfall-driven detachment and redetachment rates, flow-induced entrainment and reentrainment rates, and the deposition rate formulated as mass per unit area per unit time $[\mathrm{M/L^2/T}]$. In equation (6), representing the conservation of soil mass, β is the porosity of original soil and ρ_s is the density of solids assumed to be uniform for all sediment classes.

[11] To close the system of equations, the detachment and redetachment rates due to rainfall are calculated as [*Hairsine and Rose*, 1992]

$$e_i = F_w(1-H)p_i a_0 P, \tag{7}$$

$$e_{ri} = F_w H \frac{M_i}{M_t} a_d P, \tag{8}$$

where p_i is the ratio of the amount of sediment of class i to that of the original soil; a_0 and a_d represent detachability of uneroded and deposited soil as mass per unit volume $[\mathrm{M/L^3}]$; P is rainfall intensity $[\mathrm{L/T}]$; and $M_t = \sum M_i$ is the total sediment mass in the deposited layer in mass per unit area $[\mathrm{M/L^2}]$.

[12] The rainfall-driven detachment and redetachment rates can be relatively small under conditions where the water depth is about three times greater than the raindrop diameter [*Proffitt et al.*, 1991]; this shield effect due to flowing water is known to affect soil detachment due to raindrop impact. Consequently, a shield factor, F_w, is included in equations (7) and (8). Several forms of this factor exist including exponential relations [*Laws and Parsons*, 1943; *Mutchler and McGregor*, 1983] or a power law [*Proffitt et al.*, 1991]. Using the power law relation by *Proffitt et al.* [1991], the shield factor is formulated here as

$$F_w = \begin{cases} 1 & h \le h_0 \\ (h_0/h)^b & h > h_0 \end{cases} \tag{9}$$

where a threshold of $h_0 = 0.33 D_R$ is used, where D_R is the mean raindrop size. The exponent b varies depending on the type of soil and can be obtained with a best fit using experimental data, e.g., for clay, $b = 0.66$ [*Proffitt et al.*, 1991], and for loam, $b = 1.13$ [*Mutchler and McGregor*, 1983].

[13] The proportion of shielding of the deposited layer, H, is calculated as $H = min(M_t/(F_w M_t^*), 1)$, where M_t^* is a calibrated parameter denoting the mass of deposited sediment needed to completely sheild the original soil, given as mass per unit area $[\mathrm{M/L^2}]$. Note that the shield factor F_w is included in this relation using an analogy that the shield mass is expected to vary linearly with the rainfall redetachability, i.e., M_t^*/a_d is a constant. [*Heng et al.*, 2011].

[14] The entrainment and reentrainment rates due to overland flow are evaluated as follows [*Hairsine and Rose*, 1992]

$$r_i = (1-H)p_i \frac{F(\Omega - \Omega_{cr})}{J} \tag{10}$$

$$r_{ri} = H \frac{M_i}{M_t} \frac{F(\Omega - \Omega_{cr})}{(\rho_s - \rho_w)gh/\rho_s} \tag{11}$$

where Ω is the stream power [*Bagnold*, 1966] in units of $[\mathrm{M/T^3}]$, computed as $\Omega = \rho_w g h S_f \sqrt{u^2+v^2}$, where $S_f = n^2 (u^2+v^2) h^{-4/3}$; Ω_{cr} is the critical stream power, below which soil entrainment or reentrainment do not occur; F is the effective fraction of excess stream power in entrainment or reentrainment, which is used to account for energy dissipation due to heat; J is the specific energy of entrainment, i.e., energy required for soil to be entrained per unit mass of sediment $[\mathrm{ML^2/T^2/M}]$; and ρ_w is the density of water.

[15] Lastly, the deposition rate for a sediment class i is calculated as [*Hairsine and Rose*, 1992]

$$d_i = v_i c_i \tag{12}$$

where v_i represents the settling velocity of each sediment class $[\mathrm{L/T}]$. Two implicit assumptions of equation (12) are (i) the suspended load in the water column is completely mixed in the vertical direction [*Hairsine and Rose*, 1992], and (ii) infiltration rate does not affect settling velocities [*Tromp-van Meerveld et al.*, 2008]. The former assumption cannot be avoided because the two-dimensional H-R erosion model coupled with the vertically averaged S-V equations cannot recognize the non-uniform vertical distribution. The latter assumption is used in applications where infiltration is modeled and reflects the lack of a universal deposition equation that includes the effect of infiltrating surface since the existing forms are appropriate for a limited range of experimental conditions. This uncertainty was shown by *Tromp-van Meerveld et al.* [2008] in the form of "multiplication coefficients" that increased settling velocities for smaller particles by a factor of upto 9; the factor was ~0.35 for larger particles. No universal relationship for time-dependent infiltration rate was suggested.

[16] The coupled system of the Saint-Venant and H-R equations is therefore

$$\frac{\partial \mathbf{U}}{\partial t} + \frac{\partial \mathbf{E}}{\partial x} + \frac{\partial \mathbf{G}}{\partial y} = \mathbf{S}, \quad \frac{\partial \mathbf{M}}{\partial t} = \mathbf{D} \tag{13}$$

where $\mathbf{U}$ is the conservative variable vector, $\mathbf{E}$ and $\mathbf{G}$ are the x and y directional flux vectors, respectively, $\mathbf{S}$ is the source vector, $\mathbf{M}$ is a deposited mass vector, and $\mathbf{D}$ is the net deposition vector. These vectors are defined as

$$\mathbf{U} = \begin{pmatrix} h \\ uh \\ vh \\ c_1 h \\ \vdots \\ c_I h \end{pmatrix} \quad \mathbf{E} = \begin{pmatrix} uh \\ u^2 h + \frac{1}{2} g h^2 \\ uvh \\ c_1 uh \\ \vdots \\ c_I uh \end{pmatrix} \quad \mathbf{G} = \begin{pmatrix} vh \\ uvh \\ u^2 h + \frac{1}{2} g h^2 \\ c_1 vh \\ \vdots \\ c_I vh \end{pmatrix}$$

$$\mathbf{S} = \begin{pmatrix} S_r \\ -gh\frac{\partial z_b}{\partial x} - C_D u\sqrt{u^2+v^2} \\ -gh\frac{\partial z_b}{\partial y} - C_D v\sqrt{u^2+v^2} \\ e_1 + e_{r1} + r_1 + r_{r1} - d_1 \\ \vdots \\ e_I + e_{rI} + r_I + r_{rI} - d_I \end{pmatrix} \mathbf{M} = \begin{pmatrix} M_1 \\ \vdots \\ M_I \end{pmatrix} \quad \mathbf{D} = \begin{pmatrix} d_1 - e_{r1} - r_{r1} \\ \vdots \\ d_I - e_{rI} - r_{rI} \end{pmatrix} \tag{14}$$

[17] The resultant system of equations thus couples the hydrodynamic formulation with the advection-dominated transport equations for grain-size-dependent sediment. It expresses space-time dynamics of flow, erosion, and sediment transport.

3. Numerical Model

[18] The hydrologic model operates in a continuous fashion, simulating conditions of both storm and interstorm periods, propagating these conditions to both subsurface states and flow regimes. Consequently, hydrologic applications inevitably encounter flow conditions associated with low precipitation and runoff rates that result in many partially submerged mesh cells [*Kim et al.*, 2012b]. Tracking and handling wet and dry fronts occurring in these cells has been addressed and generally resolved by using information of neighboring wet cells [*Titov and Synolakis*, 1995; *Bradford and Sanders*, 2002; *Xia et al.*, 2010] and by modifying the bed level difference [*Brufau and Garcia-Navarro*, 2003; *Brufau et al.*, 2004]. However, such approaches were developed for hydraulic applications such as flood propagation and wave runup, and did not target hydrologic, watershed-scale applications that may have steeply sloped cells with dry conditions encountered throughout most of the simulation. As a result, these cells can cause a numerical artifact: the so called "no-flow phenomenon" that hampers an accurate calculation of the flux, bottom slope, and friction slope terms [*Kim et al.*, 2012b]. This phenomenon refers to a situation when runoff is numerically stored within a cell. Generated runoff has to fill up the cell until it becomes entirely inundated, i.e., becomes a "wet" cell. This numerical problem is critical in domains characterized by high bed slopes and low flow conditions (e.g., hillslope areas of the watershed). Previously developed shallow water models for simulating flow in rivers have not addressed this numerical problem. The tRIBS-OFM model resolved it by using a representation of the sheet flow regime; this modification significantly enhanced the accuracy of calculation of fluxes and source terms. A more detailed description of the differences between the hydrologic and hydrodynamic approaches in dealing with wet/dry situations is provided in section 2.3 of *Kim et al.* [2012b].

[19] In this study, the erosion and sediment transport equations are combined with the hydrologic and hydrodynamic formulation of tRIBS-OFM. Coupling the H-R equations to tRIBS-OFM is carried out by (i) solving them sequentially within a simulation time step for the system of equation (13) and (ii) updating the computed bed elevation at the end of time step. For torrent flow conditions with high particle concentrations, where sediment cannot be considered to be a passive admixture, a simultaneous solution of the S-V equations and H-R equations is preferable [*Cao et al.*, 2002]. As an indicator, *Cao et al.* [2002] suggested the relative time scale between the flow and deformation time scales and contended that a coupled solution is required in cases when the relative time scale is smaller than approximately 10^4. A possible flow and morphologic condition satisfying such criteria may occur in the Yellow River, China, where typical concentrations are very high, at approximately 10%, i.e., $\sim$265 kg/m^3 [*Cao et al.*, 2002]. This study, however, assumes that sediment concentrations are small enough and do not affect the movement of the fluid; the assumption is acceptable because the relative time scale is always above 10^4, except for special cases (e.g., dam-break or debris flow).

[20] The finite volume method on an unstructured grid is adopted to solve the system of equation (13). In terms of finite volume techniques, as well as computational cells and neighboring mapping functions on unstructured grids, we closely follow the approach of *Begnudelli and Sanders* [2006]. Integrating equation (13) over an arbitrary two-dimensional computational element A with a boundary Γ, the governing equations expressed in conservation form are written as follows

$$\frac{\partial}{\partial t}\int_A \mathbf{U} dA + \oint_\Gamma \mathbf{F}\cdot\mathbf{n} d\Gamma = \iint_A \mathbf{S} dA, \tag{15}$$

where $\mathbf{F}$ is the flux vector; and $\mathbf{n}$ is the unit vector normal to boundary $\partial\Gamma$ and directed outward. The integrand $\mathbf{F}\cdot\mathbf{n} = \mathbf{F}_\perp$ is the numerical flux normal to each cell face and defined as

$$\mathbf{F}\cdot\mathbf{n} = \begin{pmatrix} hu_\perp \\ huu_\perp + \frac{1}{2}gh^2\cos\varnothing + \frac{1}{24}g\Delta h^2\cos\varnothing \\ hvu_\perp + \frac{1}{2}gh^2\sin\varnothing + \frac{1}{24}g\Delta h^2\sin\varnothing \\ hc_1u_\perp \\ \vdots \\ hc_Iu_\perp \end{pmatrix} \tag{16}$$

where $u_\perp$ denotes the velocity normal to the cell interface and computed as $u_\perp = ucos\varnothing + vsin\varnothing$; $\varnothing$ is an angle between the face normal vector and the x axis; and Δh is a variation of h along the cell face. The last terms in the second and third rows of equation (16) are the hydrostatic thrust correction terms suggested by *Bradford and Sanders* [2002]. They are necessary to balance the bed slope terms for the still water condition.

[21] Among a variety of possible schemes for calculating fluxes at a cell interface between two adjacent cells, Roe's approximate Riemann solver [*Roe*, 1981] is computed using the following equation:

$$\mathbf{F}_{\perp,f} = \frac{1}{2}\left(\mathbf{F}_{\perp,L} + \mathbf{F}_{\perp,R} - \hat{\boldsymbol{R}}|\hat{\boldsymbol{\Lambda}}|\Delta\hat{\boldsymbol{V}}\right), \tag{17}$$

where the subscript f denotes the interface between two adjacent triangular cells; subscripts L and R denote left and right sides of the cell interface; and Δ denotes the finite difference across the interface. The terms $\hat{R}$ and $\hat{\Lambda}$ are the right eigenvector and the eigenvalue of the Jacobian of $\mathbf{F}_\perp$; and $\Delta\hat{V}$, defined as $\Delta\hat{V} = \hat{L}\Delta U$, denotes the wave strength, where $\hat{L}$ is the left eigenvector of the Jacobian of $\mathbf{F}_\perp$. Their mathematical representations are:

$$\hat{R} = \begin{pmatrix} 1 & 0 & 1 & 0 & \cdots & 0 \\ \hat{u} - \hat{a}cos\varnothing & -sin\varnothing & \hat{u} + \hat{a}cos\varnothing & 0 & \cdots & 0 \\ \hat{v} - \hat{a}sin\varnothing & cos\varnothing & \hat{v} + \hat{a}sin\varnothing & 0 & \cdots & 0 \\ \hat{c}_1 & 0 & \hat{c}_1 & 1 & \cdots & 0 \\ \vdots & \vdots & \vdots & \vdots & \ddots & \vdots \\ \hat{c}_I & 0 & \hat{c}_I & 0 & \cdots & 1 \end{pmatrix} \quad (18)$$

$$|\hat{\Lambda}| = \begin{pmatrix} |\hat{u}_\perp - \hat{a}| & & & & & \\ & |\hat{u}_\perp| & & & & \\ & & |\hat{u}_\perp + \hat{a}| & & & \\ & & & |\hat{u}_\perp| & & \\ & & & & \ddots & \\ & & & & & |\hat{u}_\perp| \end{pmatrix} \quad (19)$$

$$\Delta\hat{V} = \hat{L}\Delta U = \begin{pmatrix} \frac{h_R - h_L}{2} - \frac{\left((uh)_R - (uh)_L\right)\cos\phi + \left((vh)_R - (vh)_L\right)\sin\varnothing - (\hat{u}\cos\varnothing + \hat{v}\sin\varnothing)(h_R - h_L)}{2\hat{a}} \\ \left((vh)_R - (vh)_L\right)\cos\varnothing - \left((uh)_R - (uh)_L\right)\sin\varnothing - (\hat{u}\sin\varnothing + \hat{v}\cos\varnothing)(h_R - h_L) \\ \frac{h_R - h_L}{2} + \frac{\left((uh)_R - (uh)_L\right)\cos\varnothing + \left((vh)_R - (vh)_L\right)\sin\varnothing - (\hat{u}\cos\varnothing + \hat{v}\sin\varnothing)(h_R - h_L)}{2\hat{a}} \\ (c_1 h)_R - (c_1 h)_L - \hat{c}_1(h_R - h_L) \\ \vdots \\ (c_I h)_R - (c_I h)_L - \hat{c}_I(h_R - h_L) \end{pmatrix} \quad (20)$$

where a denotes the celerity of a simple gravity wave; and $u_\parallel$ denote the velocity components parallel to the cell interface and are computed as $u_\parallel = -u\sin\varnothing + v\cos\varnothing$. The quantities denoted with a hat are Roe averages, which are calculated with the following relations:

$$\hat{h} = \sqrt{h_L h_R}, \hat{u} = \frac{\sqrt{h_L}u_L + \sqrt{h_R}u_R}{\sqrt{h_L} + \sqrt{h_R}}, \hat{v} = \frac{\sqrt{h_L}v_L + \sqrt{h_R}v_R}{\sqrt{h_L} + \sqrt{h_R}}, \\ \hat{a} = \sqrt{\frac{g}{2}(h_L + h_R)}, \hat{c}_i = \frac{\sqrt{h_L}c_{i,L} + \sqrt{h_R}c_{i,R}}{\sqrt{h_L} + \sqrt{h_R}}. \quad (21)$$

[22] Since Roe's method does not calculate the correct flux for critical flow, a local depression wave is introduced at critical flow locations by replacing the first and third eigenvalues with the following equation [*Hirsch*, 1990]:

$$|\lambda|^* = \frac{\lambda^2}{\Delta\lambda} + \frac{\Delta\lambda}{4}, \quad (22)$$

where $\Delta\lambda = 4(\lambda_R - \lambda_L)$. This relation is used when $-\Delta\lambda/2 < |\lambda| < \Delta\lambda/2$ and the other eigenvalues, $\lambda = |\hat{u}_\perp|$, remain unmodified.

[23] Under the assumption that all source terms in the flow and erosion equations are constant within a cell triangle, they are calculated as

$$\iint_A \mathbf{S}dA = \mathbf{S} \cdot A, \quad (23)$$

[24] In the computation of the bottom slope, the gradient of z_b is obtained by applying Green's theorem to transform the area integral to the line integral. Thus, the integration of z_b along the cell boundaries gives

$$\frac{\partial z_b}{\partial x} = \frac{(y_2 - y_0)(z_1 - z_0) - (y_1 - y_0)(z_2 - z_0)}{(y_2 - y_0)(x_1 - x_0) - (y_1 - y_0)(x_2 - x_0)}, \quad (24)$$

where the subscripts 0, 1, and 2 are three counterclockwise vertices of a cell triangle. All variables used for computations of source terms are evaluated at the cell center.

[25] Finally, equations (13) and (6) are solved by using the following update equation

$$\mathbf{U}_j^{t+\Delta t} = \mathbf{U}_j^t + \Delta t\left[-\frac{1}{A_j}\sum_{k=1}^{3}\mathbf{F}_{\perp_{j,k}} l_{j,k} m_{j,k}\right]^t + \Delta t \cdot \mathbf{S}_j^{t*}, \quad (25)$$

$$\mathbf{M}_j^{t+\Delta t} = \mathbf{M}_j^t + \Delta t \cdot \mathbf{D}_j^t, \quad (26)$$

$$z_{b_j}^{t+\Delta t} = z_{b_j}^t + \frac{\Delta t}{(1-\beta)\rho_s}\left[\sum_{i=1}^{I}\left(d_{i,j} - e_{i,j} - e_{ri,j} - r_{i,j} - r_{ri,j}\right)\right]^t \quad (27)$$

where j and k are cell and face indexes, respectively, $l_{j,k}$ is the length of the k-th face of the i-th cell, and $m_{j,k}$ is a function that takes on values of 1 or -1, depending on whether the unit vector normal to the k-th face of the i-th cell is directed outward or inward. The t^* superscript in equation (25) represents that for stability, the friction and deposition terms including the conservative variables are treated in a semi-implicit manner, while rest of the source terms are treated explicitly [*Sanders*, 2008].

[26] Several types of boundary conditions can be imposed by either placing extrapolated quantities in a "ghost" cell adjacent to the boundary or directly specifying a given flow depth or a discharge. These extrapolated or specified quantities defined for ghost cells are employed to calculate boundary fluxes necessary in Roe's Riemann solver. At a solid slip wall boundary, water depth and concentrations are extrapolated; velocities are specified in ghost cells that require the velocity normal to the cell interface to be zero while the velocity parallel to the interface remaining unchanged. If water flows into a domain through an inflow boundary, for subcritical flow only $(I+2)$ boundary conditions are needed among the $(I+3)$ possible variables that include depth (h), two velocities (u, v), and concentrations (c_i–s, $i = 1 \ldots I$), where I is the number of sediment size classes. Any two flow variables and concentrations need to be specified while the remaining flow variable is extrapolated from a value adjacent to the boundary.

Table 3. Simulation Conditions and Parameters for Aridisol (Solonchak) After *Sander et al*. [1996]

Case	Rainfall (mm/h)	Slope	Depth (m)	a_0 (kg/m^3)	a_d (kg/m^3)	M_t^* (kg/m^2)
1	100	0.01	0.002	1233	24,660	0.0493
2	100	0.04	0.005	718	14,360	0.0598
3	100	0.03	0.01	412	8240	0.0515

A supercritical inflow through the boundary needs all $(I+3)$ boundary conditions. For a boundary where flow leaves the domain, a subcritical flow needs one boundary condition (in this study, in the form of free outfall or zero-depth gradient boundary condition), while no boundary condition is needed for a supercritical flow.

[27] The proposed model is based on an explicit time integration scheme and thus a stability restriction, the Courant-Friedrichs-Lewy (CFL) condition, must be satisfied in each cell. For a triangular mesh, the time step Δt in the model is defined as [*Begnudelli and Sanders*, 2006]:

$$Cr = \Delta t \cdot \max_{j=1,2,\ldots N_c}\left\{\frac{3\max_{k=1,2,3}|\lambda_{j,k}{}^{\perp} l_{j,k}|}{A_j}\right\} \leq 1,\ j = 1, 2, \ldots N_c \tag{28}$$

where Cr is the Courant number, N_c is the number of cells, and $\lambda_{j,k}{}^{\perp}$ is the wave speed normal to the k-th face of the j-th cell. Furthermore, the restriction on the time step presented by *Heng et al*. [2009] is also considered. Specifically, negative concentrations should not be generated and an approximate estimate of the corresponding time step is

$$\Delta t \leq \frac{\min_{j=1,2,\ldots N_c}(h_j)}{\max_{i=1,2,\ldots I}(v_i)}. \tag{29}$$

[28] This relation usually limits the time step because it yields estimates that are smaller than those obtained with the CFL criteria.

4. Model Verification

4.1. Rainfall-Induced Erosion

[29] One of the two significant contributors to the process of erosion represented in the H-R model is rainfall-induced erosion. The problem has been addressed with many methods: a steady state solution [*Hairsine and Rose*, 1991], unsteady but spatially independent solutions [*Sander et al*., 1996; *Parlange et al*., 1999], an event-based solution [*Hairsine et al*., 1999], and temporally spatially dependent solutions [*Hogarth et al*., 2004a; *Heng et al*., 2009]. Most of these analytical or numerical solutions were compared with experimental data by *Proffitt et al*. [1991] and demonstrated a good agreement. Experimental results obtained by *Proffitt et al*. [1991], specifically, observations for Aridisol soil are used in this study for verification of numerical solutions of the coupled model. An approximate analytical solution developed by *Sander et al*. [1996] is also used for a comparison. Although this unsteady analytical solution assumes that the sediment concentration does not vary spatially and is only time dependent near the end of the flume, and thus neglects the spatial derivative terms, the effects of the assumption are minor and the accuracy of the analytical solution is trustworthy, except at very short times [*Hogarth et al*., 2004a].

[30] Simulation conditions and parameters providing the best agreement with experimental data for the case of Aridisol are borrowed from *Sander et al*. [1996] and listed in Table 3. The value of the Manning coefficient is 0.06 s/m$^{1/3}$ and for Aridisol, with a slightly dispersive soil of sandy clay loam texture, 10 sediment sizes are used; the corresponding settling velocities, $v_{1,\ldots,10}$, are 0.0035, 0.07389, 0.5194, 2.1, 6.8, 20, 38, 75, 160, and 300 mm/s [*Parlange et al*., 1999]. A shield effect factor F_w equal to 1.0 is used. The simulation domain consists of 5.8 × 1 m and the size of triangular mesh elements is 0.005 m^2. The number of mesh nodes and cells are 654 and 1170, and the time step used for the simulation period of 50 min is 0.05 s. The density of sediment material solids is 2600 kg/m^3. Hydrologic processes are not considered in this problem.

[31] The temporal distributions of the flow discharge, the sediment discharge, and the total concentration at the downstream end of the hillslope for the three simulation cases are shown in Figures 1 and 2. Hydrographs initially show different peaks due to the differences in transient flow conditions, but eventually approach the same steady state due to the same rainfall intensity. Sedigraphs also approach a steady state, but a higher sediment discharge occurs in case 1 because of the high erodibilities of uneroded and deposited soil. In Figure 2, the total sediment concentrations exhibit behaviors similar to that of the sedigraphs. An overall good agreement with the experimental data by *Proffitt et al*. [1991] and the analytical solution by *Sander et al*. [1996] can be observed.

[32] The time series showing size-selective characteristics at the hillslope bottom for simulation case 2 are provided in Figure 3 showing how sediment particles of different size contribute to the deposited mass and water column concentration. Specifically, larger particles tend to contribute a higher fraction of the deposited mass, but contain less sediment in water column than smaller particles. This result also agrees well with the analytical solution by *Sander et al*. [1996]. As can be inferred from equations (7) and (8), because of an equally distributed ratio of each sediment class in the original soil, the simulated detachment rates exhibit uniform detachment for each sediment class, while a size-selective distribution ratio of the deposited soil (Figure 3a) results in a size-selective redetachment (not shown). After a short period of time, the original intact soil becomes almost completely covered by the deposited sediment and the shielding proportion H nearly approaches 1.0. As follows, most of the detachment occurs during an early time period. The supporting information provides further analysis of size-specific spatial distributions of sediment concentrations deposited mass at different simulation times (see section S1).

4.2. Overland Flow-Induced Erosion

[33] In order to evaluate and verify the overland flow-induced erosion component of the H-R model, a sediment-laden overland flow problem [*Beuselinck et al*., 1999; *Sander et al*., 2002; *Heng et al*., 2009] is presented. An overland flow rate of 0.00125 m^3/s is imposed at the hillslope upstream boundary; concentrations of 10 kg/m^3 are

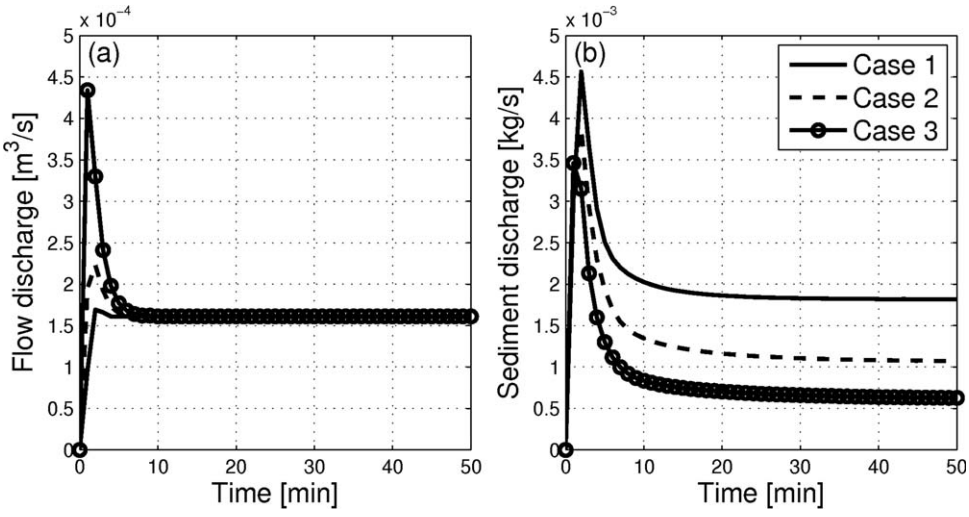

Figure 1. Simulated (a) hydrographs and (b) sedigraphs for three cases in the rainfall-induced erosion problem.

specified for all sediment classes, which results in a net deposition of sediment over the domain. The parameter values are specified as follows: the Manning coefficient is 0.01 s/m$^{1/3}$, the critical stream power is 0.18639 W/m^2, the effective fraction of excess stream power is 0.01, the slope of domain is 0.02, the density of sediment is 2600 kg/m^3, and the settling velocities, $v_{1,\cdots,10}$, are 0.00043, 0.0037, 0.02, 0.083, 0.23, 0.46, 0.74, 1.1, 1.7, and 3.2 mm/s, respectively. The simulation domain has the dimensions of 10 m $\times$ 1 m and the size of mesh elements is 0.005 m^2. The number of mesh nodes and triangular cells are 1116 and 2010, respectively. The time step used during the simulation period of 6 min is 0.005 s. Hydrologic components are not considered in this problem.

[34] The flow imposed as a boundary condition reaches the outlet and the system achieves steady state almost immediately (not shown). The total sediment yield at the outlet contains primarily finer particles, as compared to coarser sediments. This is consistent with a theoretical understanding of overland flow erosion: lighter soil particles are more easily moved away from their sites of origin, as compared to slowly moving heavier particles. The spatial distributions of concentrations and mass fractions of each sediment class at steady state are compared with an analytical solution of *Sander et al*. [2002] in Figure 4. Although small differences are present in the simulated concentrations of larger particles near the upstream end, an overall good agreement of the simulation results with the analytical solution can be observed. The observed differences might be due to the boundary condition effect and the kinematic approximation of the flow motion. Specifically, only constant q and c_i are available as the inflow boundary condition [*Sander et al*. 2002] and thus, the specification of an additional boundary condition is required for the 2-D formulation. We assumed the depths for external "ghost" cells from the estimation of the kinematic wave solution, using the power of 5/3 for turbulent flow. As a result, the simulated values for h and u at internal cells near the boundary may slightly deviate from the flow state in *Sander et al*. [2002] using the kinematic approximation.

[35] The supporting information provides additional analyses of size-specific spatial distributions of sediment concentrations and deposited mass at different simulation times (see section S.1).

4.3. Lucky Hills Watershed

[36] Despite their numerical formulation, the previous two simulation cases are in fact one-dimensional. The perceived strength of the developed model is however in the potential to represent the coupled hydrology, flow hydrodynamics, physically based erosion, and sediment transport dynamics of more complex domain geometries. Yet no analytical solutions or suitable laboratory observations are available for relevant model confirmation. A real-world watershed is used as a case study for investigating the two-dimensional capabilities of the proposed model. Specifically, the Lucky Hills watershed, nested within the Walnut Gulch Experimental Watershed (WGEW), southeastern Arizona, USA, was selected because the WGEW sediment

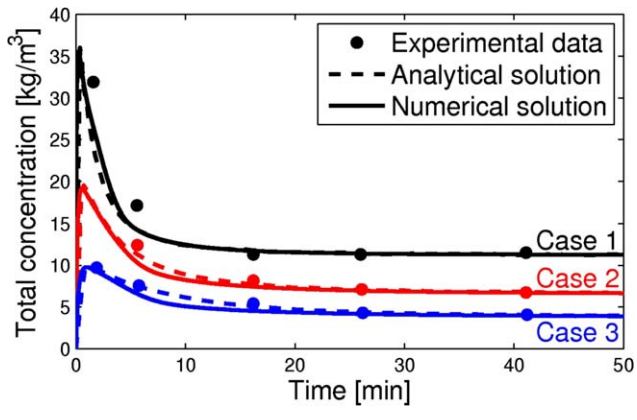

Figure 2. The time series of the total sediment concentration at the hillslope bottom for three cases considered in the rainfall-induced erosion problem. "Experimental data" refer to the measurements by *Proffitt et al*. [1991] and "Analytical solution" refers to *Sander et al*. [1996].

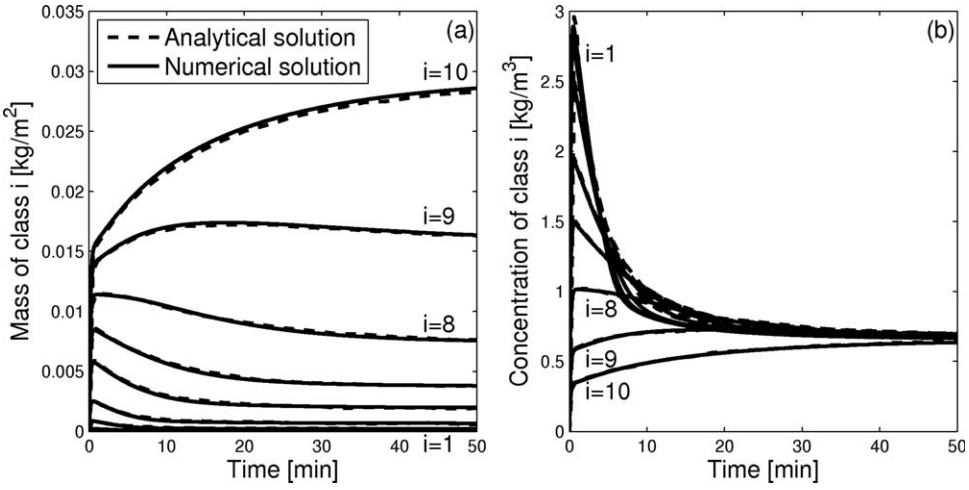

Figure 3. The time series of (a) deposited masses and (b) concentrations of each sediment class at the hillslope bottom for the simulation case 2 of the rainfall-induced erosion problem; $i = 1$ corresponds to smallest sediment particles and $i = 10$ refers to largest particles.

collection program provides an extensive experimental data set obtained with automatic traversing slot samplers [*Renard et al*., 1986].

[37] The area of the watershed is 36,800 m^2 and its elevation ranges from 1364 to 1375 m above sea level. The overall slope of the basin is less than 10%; however, there are abrupt changes of elevation (~10 m) and high slopes (higher than 20%) near the center of the domain (see Figures 5a and 5b). This morphological feature can be expected to affect the spatial variability of erosion rates and will be discussed later. One version of a refined mesh is shown in Figure 5c. It is defined according to the convergence of surface flow contributing area (CA) illustrated in Figure 5d. This refined domain will be used to explore the sensitivity of hydrograph and sedigraph to the mesh resolution.

[38] Average annual precipitation is about 300 mm and 70% of precipitation falls during the summer monsoon. Typical storms in the area have a short duration and a high intensity. For the calculation of the shield effect factor, the mean raindrop size is assumed to be 2 mm and the exponent b in equation (9) is assumed to be 1.0 [*Heng et al*., 2011]. The dominant vegetation is desert shrub and semi-arid rangeland plants.

4.3.1. Sensitivity to Representation of Particle Size Distribution and Surface Topography

[39] The dominant soil type in the Lucky Hills watershed is McNeal Gravelly Sandy Loam [*Francipane et al*., 2012]. The density of sediment is 2700 kg/m^3; porosity of bed equal to 0.46 is used [*Francipane et al*., 2012].

[40] The determination of the number of particle sizes (I) is of great importance for representing size-selective characteristics of the erosion process. For this watershed, the empirical particle size distributions (PSDs) were obtained with 23 sieves (3, 6, 11, and 3 of them corresponded to the range of clay, silt, sand, and gravel particles, respectively)

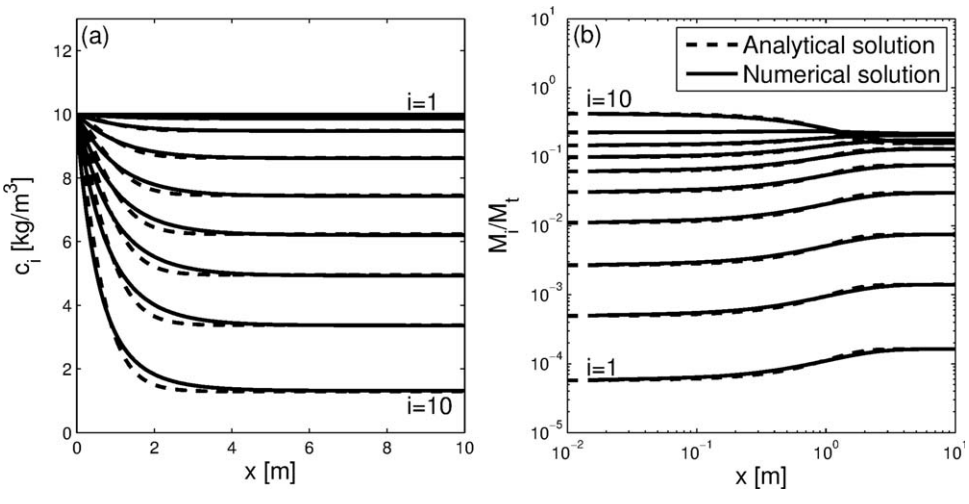

Figure 4. A comparison of (a) the sediment concentrations and (b) the mass fractions of each sediment class with the analytical solution of *Sander et al*. [2002]. A steady state situation for a case of net deposition in overland flow is considered.

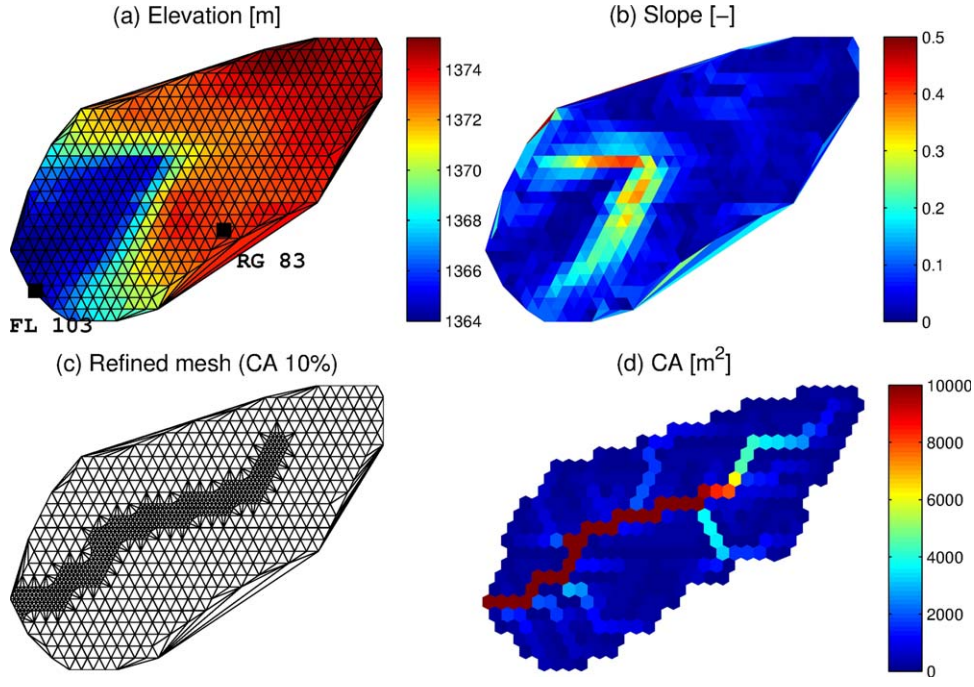

Figure 5. (a) The digital elevation model and (b) the derived surface slope of the Lucky Hills watershed. Precipitation is measured at the rain gauge RG83. Runoff and sediment are measured at the outlet flume FL103. Two types of computational mesh are shown: (Figure 6a) coarsest mesh and (c) refined mesh (CA 10%). The latter is a refined version of the former in the channel area, where (d) the surface contributing area is greater than 10% of the total contributing area of the watershed.

at six different locations (Schaap and Shouse, unpublished manuscript, 2013). To investigate the effect of the number of particle sizes on the generated sediment yield (SY), the distribution with 23 intervals (obtained by averaging data for six locations) was recomputed into distributions containing 4, 8, and 12 intervals. These distributions were used to compute particle settling velocities (Figure 6).

[41] The results presented in Figure 7 illustrate sensitivity of hydraulic and erosion simulations to the number of particle sizes and the mesh resolution for the Lucky Hills watershed. The results correspond to the same parameter values obtained through calibration, as described in the following. Specifically, a first parameter set was obtained from a preliminary simulation using the particle size distribution with four intervals and the coarsest mesh to represent the watershed; two sensitivity tests were carried out using these parameter values; PSD with eight size intervals and the coarsest mesh were identified as an appropriate control case; the parameters were recalibrated based on the control case (as described in the section 4.3.2); and the sensitivity results were recomputed and presented in Figure 7.

[42] Figure 7a shows the ratios of modeled sediment yields with respect to SY obtained in simulation with 23 particle sizes. The results imply that the coarse representation of PSD gives rise to considerable size-dependent variations that are more pronounced for the coarser particles, e.g., reaching up to ~60% for SY of sand. However, since the ratio of SY of finer particles to the total SY is much greater than that of the coarser particles, the total yields for the four representations of PSD do not vary significantly (e.g., up to ~5% from the maximum for $I = 4$). Consequently, the PSD with eight intervals is used for computational efficiency in simulations that explore hydrogeomorphic behavior of the watershed. The respective sediment sizes for eight intervals are 0.001191, 0.002687, 0.01555, 0.04469, 0.2876, 1.131, 3.399, and 5 mm; their corresponding fractions are 6.87, 3.33, 5.42, 4.77, 21.54, 18.39, 20.90, and 18.78%; the settling velocities, $v_{1,\ldots,8}$, 0.0009823, 0.005001, 0.1669, 1.352, 32.89, 124.3, 252.2, and 313.6 mm/s, are calculated using the formula of *Cheng* [1997].

[43] Maintaining an appropriate spatial resolution for the simulation domain also has an important role for representing the important features of hydrogeomorphic dynamics. Specifically, a poorly resolved mesh near the channel network (as opposed to hillslopes) can lead to a significant impact on the computation of wave speed and therefore the watershed time of concentration [*Kim et al*., 2012b]. Similarly to the previous study of *Kim et al*. [2012b], we test the hydrograph and sedigraph sensitivity in terms of their total volume/yield, peak rate, and time to peak for six refined meshes. The "coarsest" mesh consists of isosceles triangles, each of which has an area of 50 m^2; the number of mesh nodes and triangular cells are 469 and 908 (Figure 5a); the "finest" mesh is also composed of isosceles triangles that are nine times smaller than triangles of the coarsest mesh (not shown). Using the conclusion of *Kim et al*. [2012b] concerning mesh resolution sensitivity, the other four meshes are only refined near the channel area, where the flow concentration is expected to be higher according to the accumulation of the contributing area (Figure 5d). As

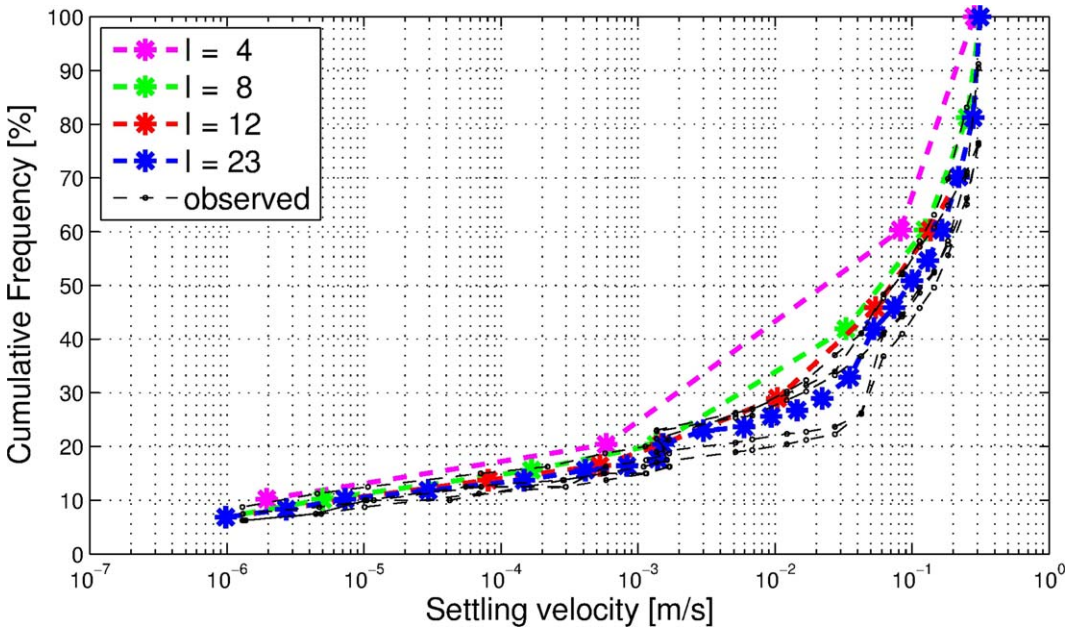

Figure 6. The settling velocities computed from particle size distributions reported for six locations within the Lucky Hills watershed (black lines) and recomputed settling velocities used in simulations with different *I*s. The "*I*" denotes the number of sediment size classes.

an example, Figure 5c shows the mesh refined for the area where the surface CA is greater than 10% of the total CA (called "CA 10%").

[44] In the corresponding simulations, the time step used for hydrologic components (Table 2) is 3.75 min; the time step used for the simulation of flow hydrodynamics and erosion-transport modeling components is 0.01 s. Figure 7b shows the sensitivity of the ratio of several metrics computed in simulations with refined meshes with respect to results obtained for the coarsest mesh. As expected, the simulation central processing unit (CPU) time grows significantly as the number of cells/nodes increases: for the coarsest mesh, the wall-clock simulation time for a 3 h rainfall event is 264 min in a serial mode using Intel Xeon CPU (3.33 GHz, L2 cache 8M) with 14 GB DDR3 RAM. In contrast, the accuracy of simulation of physical variables, i.e., the total volume and yield, the magnitudes of hydrograph and sedigraph peaks, and the times to peak are not significantly affected by the domain resolution. In terms of the times to peak, the results are consistent for all mesh types; the maximum deviations of SY and peak of sedigraphs are 5 and 12%, respectively, and that for flow volume and peak of hydrographs are 1 and 2%, respectively. This implies that the sediment-related simulation results are more sensitive to the mesh resolution, as compared to the metrics describing water flow. The likely reason is that sediment dynamics are affected by a larger number of parameters that can result in resolution-related dependencies, as compared to flow influenced by a single friction parameter. Hereafter, due to the marginal deviations of output physical variables, we will exploit higher computational efficiency of the coarsest mesh in the rest of simulations.

4.3.2. Model Calibration and Confirmation

[45] An extensive data set on precipitation, runoff, and sediment yield has been collected at WGEW since the mid-

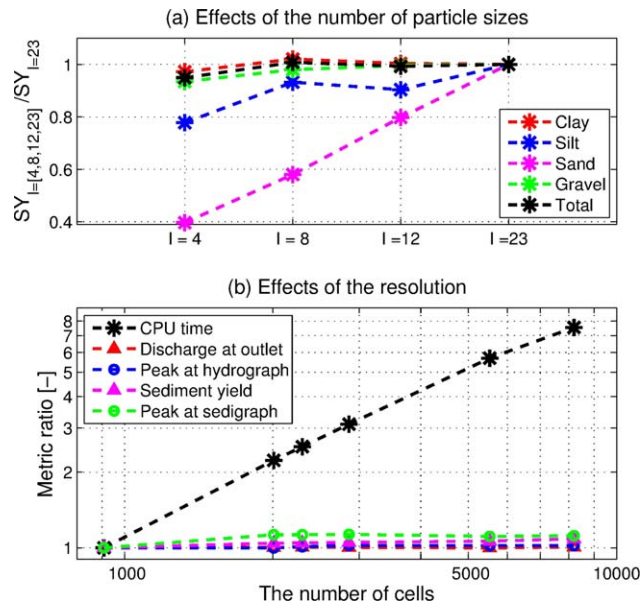

Figure 7. Sensitivity of hydraulic and morphologic behaviors to the number of particle sizes (*I*) and the domain mesh resolution: (a) the ratios of the total sediment yield for four representations of sediment textural composition ($I = 4$, 8, 12, and 23) with respect to that of $I = 23$; (b) the ratio of several simulation metrics (see the figure legend) for six meshes with respect to those of the coarsest domain. Starting from left, the points correspond to the domain coarsest, CA 10%, CA 7%, CA 4%, CA 1%, and finest resolutions that contain 908, 2010, 2298, 2858, 5524, and 8192 triangular cells, respectively.

Table 4. A Summary of Observed Rainfall, Runoff, and Sediment for Events Used in Simulations for the Lucky Hills Watershed[a]

Event		Observed Rainfall			Observed Runoff and Sediment				Simulation	
No.	Date	Start Time	Duration (min)	Depth (mm)	Start Time	Duration (min)	Volume (m^3)	Sediment Yield (kg)	Start Time	Duration (min)
1	10 Aug 2000	15:40	37	26.289	15:42	53	414.736	9933	14:45	180
2	4 Aug 2002	12:52	34	28.956	12:54	61.25	379.04	7426	12:00	180
3	23 Aug 2003	14:39	16	17.780	14:42	50	230	7092	13:45	180
4	27 Jul 2005	18:40	169	22.987	19:07	44.5	44.528	1623	17:45	240
5	8 Sep 2005	12:17	73	38.735	12:15	109.25	614.56	15,831	11:30	180
6	23 Jul 2007	13:20	14	14.224	13:21	34.75	110.032	3301	12:30	180
7[b]	31 Jul 2007	15:34	126	41.656	15:35	87.75	516.304	16,027	14:45	180
8	9 Sep 2007	15:52	115	16.129	17:28	35.5	167.808	5244	15:00	360
9	19 Jul 2008	21:27	311	46.355	21:27	115	484.288	11,215	20:30	360
10	25 Jul 2008	14:36	42	30.226	14:37	81.25	476.56	9892	13:45	180

[a]Rainfall was measured at "Gage 83." Runoff and sediment were measured at flume "FL103."
[b]Event 7 is used for calibration.

dle 1950s (http://www.tucson.ars.ag.gov/dap/) [*Goodrich et al.*, 2008; *Nichols et al.*, 2008; *Stone et al.*, 2008]. Data since 1999, when precipitation and runoff data collection programs were updated with new sensors, are used in this study. Ten precipitation events for which runoff and sediment data are available were chosen for calibration and verification of the numerical model with the same initial conditions of dry domain and intact soil. These events are summarized in Table 4.

[46] Calibration of a numerical model that requires multiple parameters to represent physical phenomena is a challenging task. As described in section 2, the parameters are grouped according to their primary effect in simulating hydrologic (tRIBS), hydraulic (OFM), or sediment erosion-transport dynamics (H-R equations). Approximately 70% of the parameters in Table 5 are used to represent hydrological processes. Among them are (1) soil hydraulic properties (nine parameters) associated with the processes of infiltration and runoff production. These parameters play a key role in simulating soil moisture, flow, and erosion because they control the magnitude and timing of hydraulic and morphologic responses to precipitation. Two of the nine parameters, the saturated hydraulic conductivity (K_s) and the conductivity decay parameter (f) were chosen as primary in model calibration to match the observed flow behavior. The accepted understanding in this calibration strategy is that a higher value of f can lead to a larger magnitude of infiltration-excess runoff, preclusion of

Table 5. Parameters Used to Represent Hydrologic, Hydraulic, and Sediment Erosion-Transport Dynamics of the Lucky Hills Watershed[a]

Parameter	Description	Value	Unit	Source	Usage
$\boldsymbol{n}$	Manning coefficient	0.033	$s\ m^{-1/3}$	C	Flow
a_0	Detachability of original soil	80	$kg\ m^{-3}$	C	Erosion
a_d	Detachability of deposited soil	2000	$kg\ m^{-3}$	C	Erosion
$\boldsymbol{F}$	Effective fraction of excess stream power	0.01		C	Erosion
Ω_{cr}	Critical stream power	0.12	$W\ m^{-2}$	L	Erosion
$\boldsymbol{J}$	Specific energy of entrainment	189.06	$m^2\ s^{-2}$	L	Erosion
M_t^*	Deposited mass needed to sheild original soil	2.7	$kg\ m^{-2}$	C	Erosion
K_S	Saturated hydraulic conductivity	20.0	$mm\ h^{-1}$	C	Soil-hydraulic
θ_S	Volumetric soil moisture at saturation	0.39	$m^3\ m^{-3}$	L	Soil-hydraulic
θ_R	Volumetric residual soil moisture	0.0463	$m^3\ m^{-3}$	L	Soil-hydraulic
$\boldsymbol{m}$	Pore-size distribution index	0.3813		L	Soil-hydraulic
φ_B	Air entry bubbling pressure	−63	mm	L	Soil-hydraulic
$\boldsymbol{f}$	Conductivity decay parameter	0.03	mm^{-1}	C	Soil-hydraulic
A_S	Anisotropy ratio in the saturated zone	1		L	Soil-hydraulic
A_u	Anisotropy ratio in the unsaturated zone	1		L	Soil-hydraulic
η'	Bedrock depth	50	m	L	Soil-hydraulic
k_s	Volumetric heat Conductivity	0.214	$J\ m^{-1}\ s^{-1}\ K^{-1}$	L	Soil-thermal
C_s	Soil heat capacity	1,209,573	$J\ m^{-3}\ K^{-1}$	L	Soil-thermal
$\boldsymbol{S_s}$	Canopy storage	1	mm	L	Storage
$\boldsymbol{B}$	Interception coefficient	0.2		L	Storage
$\boldsymbol{p}$	Free throughfall coefficient	0.35		L	Interception
$\boldsymbol{S_c}$	Canopy field capacity	1	mm	L	Interception
$\boldsymbol{K}$	Canopy drainage rate coefficient	0.18	$mm\ h^{-1}$	L	Interception
$\boldsymbol{g_d}$	Canopy drainage exponent	3.9	mm^{-1}	L	Interception
$\boldsymbol{alb}$	Surface albedo	0.22		L	Veg.-thermal
$\boldsymbol{H_v}$	Vegetation height	0.46	m	L	Veg.-thermal
$\boldsymbol{K_t}$	Optical transmission coefficient	0.7		L	Veg.-thermal
$\boldsymbol{r_s}$	Canopy average stomatal resistance	200	$s\ m^{-1}$	L	Veg.-thermal
$\boldsymbol{V_f}$	Vegetation fraction	0.5		L	Veg.-thermal

[a]The letter "C" refers to the parameters whose values were calibrated; "L" refers to the parameters whose values were inferred from literature.

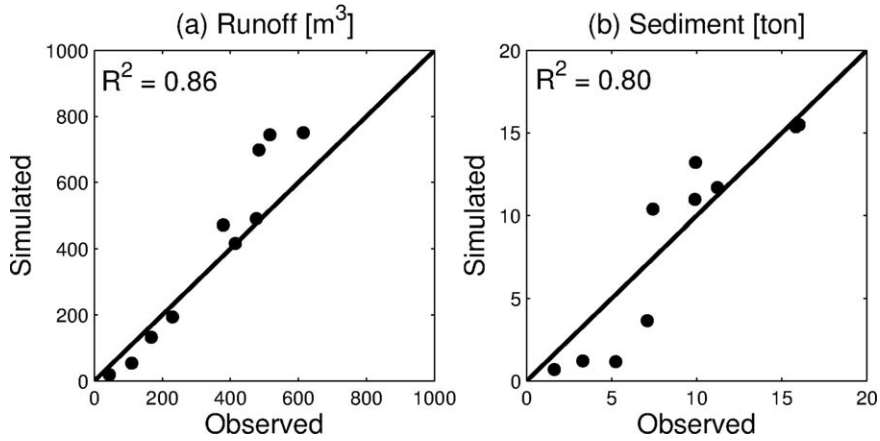

Figure 8. A comparison of the simulated and observed (a) runoff volumes and (b) sediment yields for 10 selected events. R^2 denotes the determination coefficient, which was computed by using nine data points (excluding data for event 7, i.e., the calibration case).

groundwater exfiltration, a faster basin response in time to peak, and a more rapid hydrograph recession. A more conductive soil (i.e., higher K_s) will generate less runoff and respond slower response to rainfall. (2) Soil thermal properties and vegetation characteristics (seven parameters) related to evapotranspiration and energy balance that determine the magnitude of surface energy fluxes such as short/long wave radiation and latent/sensible/ground heat flux, and evapotranspiration components. (3) Vegetation interception parameters (six parameters), which influence the storage capacity and canopy dynamics of moisture in the canopy water balance model [*Rutter et al*., 1971; *Rutter et al*., 1975]. The latter two groups of thermal and interception parameters were not calibrated in this study because the associated effects are minor at the event scale. The same parameter values as in *Francipane et al*. [2012] were used for this watershed as they resulted in a good agreement with the observed runoff data for a 10 year simulation period from 1999 to 2009. A more detailed description of the calibration methodology for hydrologic components is provided in *Ivanov et al*. [2004a] and includes a description of the relative importance of parameters and spatiotemporal aspects of calibration.

[47] Only a single parameter reflecting bed roughness conditions needs to be calibrated for the Saint-Venant equations. This friction parameter is well known to influence the timing and peak of hydrograph and thus has a high priority in calibration. A proper value of the parameter is usually determined either by referring to literature or estimated from regression equations such as those in [*Kim et al*., 2012a], when the flow surface represents emergent vegetation or obstacles. Higher values of the friction coefficient retard the simulated flow, resulting in smaller peak magnitude and time to peak. In this study, the Manning resistance coefficient was manually calibrated using event 7 (Table 4) by matching the measured and simulated flow hydrograph characteristics at the basin outlet.

[48] In terms of parameters of H-R equations, four out of six major parameters (Table 5) were calibrated by matching the measured and simulated sediment yield for the same event. The effort of calibrating the parameters of specific energy of entrainment and critical stream power was reduced by using two relationships suggested by *Heng et al*. [2011]:

$$J = \frac{0.5\rho_w {v_R}^2}{a_0} \text{ and}$$
$$\Omega_{cr} = 5.74\rho_w \left(\theta_c D_{50} g \frac{\rho_s - \rho_w}{\rho_w}\right)^{3/2} \log\left(12.3 \frac{\theta_c}{S} \frac{\rho_s - \rho_w}{\rho_w}\right), \tag{30}$$

where v_R is the velocity of rainfall impact assumed to be 5.5 m/s, θ_c is the critical Shields parameter for incipient motion equal to 0.045, D_{50} is the median particle size, and S is the domain slope. The number of manually managed, replicate simulations was less than 100. The final values of the parameters used in the simulations are presented in Table 5.

[49] By using the parameter values obtained through calibration for event 7, the total watershed runoff volumes and sediment yields were calculated for 10 selected events (Table 4). The results were compared with observations and are shown in Figure 8. For relatively large events, the simulated values tend to be overestimated, while for smaller events they are somewhat underestimated. Despite these discrepancies, the comparison is very satisfactory: the determination coefficients of $R^2 = 0.86$ for runoff and $R^2 = 0.80$ for sediment were obtained (Figure 8). The discrepancies may be due to employed assumptions and inherent uncertainties: (1) soil and land use characteristics used in tRIBS are assumed to be spatially uniform over the entire basin; (2) precipitation is also assumed to be spatially uniform and data were aggregated to a 15 min resolution from a 1 min resolution [*Francipane et al*., 2012], which may affect runoff production; (3) the hydrological parameters were calibrated over a period of 10 years, with the final tendency of generating a slightly higher runoff for large events.

[50] Figure 9 shows the time series of flow and sediment fluxes for events 2 and 7. Since observations do not provide the actual time series of sediment flux, the observed data shown in the sedigraphs were computed using information on sediment concentration and flow volume flux. As seen, the measured and simulated flow rates at the outlet exhibit a very good match. The two sediment discharge series,

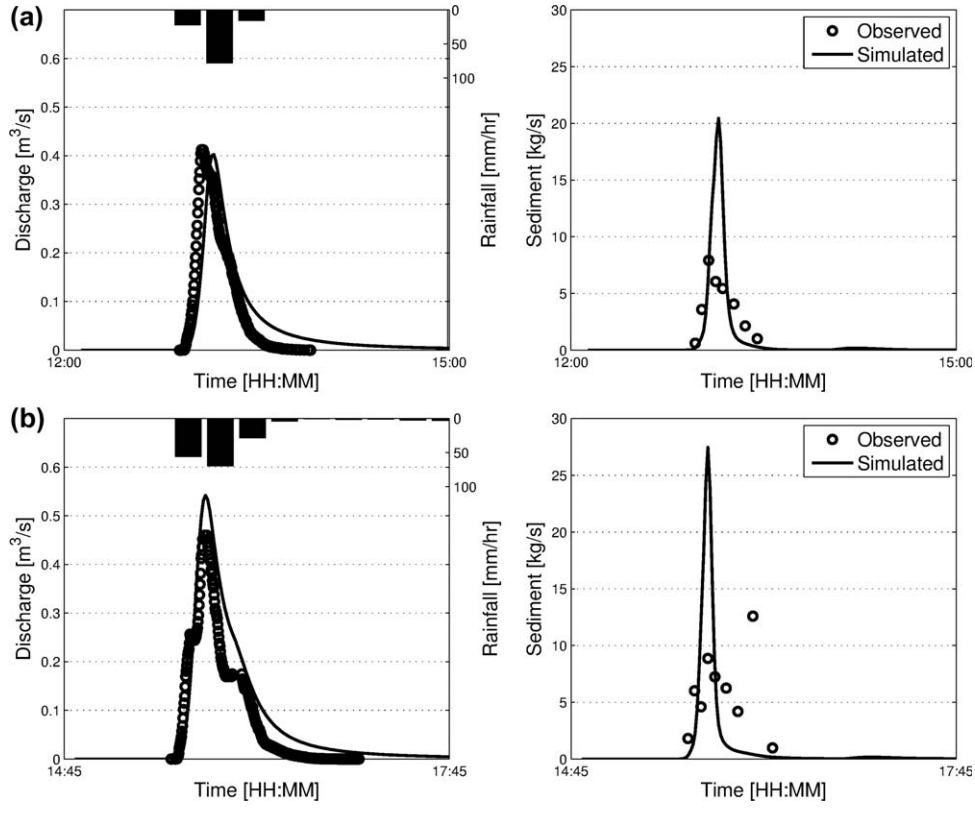

Figure 9. Hydrographs and sedigraphs for (top) event 2 and (bottom) event 7.

however, are not in a perfect agreement even though the total sediment volumes are almost identical (see Figure 8). The reason for that could be due to the fact that sediment concentration was measured in an intermittent manner (~10 times during a given event), as compared to flow measurements (~100 times per event). The episodic nature of concentration measurements might have failed to capture abrupt changes during periods of high sediment yield. Inasmuch as a real-time measurement of a sedigraph is difficult and errors are inevitable, the deviation between the observed and simulated sedigraphs can be appreciated.

4.3.3. Spatial Characteristics of Flow and Erosion Processes

[51] Figure 10 illustrates the simulated spatial distributions of depth, velocity, total concentration, and elevation changes over the basin, and compares them for simulation hours 1 and 2 (event 7). The time of 1 hour corresponds to the occurrence of the observed flow peak and the time of 2 hours corresponds to the flow recession period. As expected, higher depths, velocities, and concentrations can be observed near the peak time, as compared to those during the recession period. Elevation changes are such that most of the watershed area is being eroded, except for a confluence area, where there is an abrupt morphological transition from steep to mild slopes (Figures 5 and 10). Furthermore, sharp variations in the distributions of total concentration (especially for the larger particles) and elevation change can be detected in that same area. In order to address these variations from a mechanistic point of view, an inspection of the governing equations for possible driving reasons is necessary.

[52] Erosion processes represented by the source terms in the H-R equations indicate that major factors affecting the spatial variation of sediment variables are two flow variables: depth and velocity (equations (7), (8), and (10)–(12)). Since the rates of erosion in equations (10) and (11) are directly proportional to flow velocity and those in equations (11) are inversely proportional to depth, the ratio of these variables is used in Figure 11a. The figure shows change in elevation as a function of the ratio for all computational cells at hour 1. Another independent variable, the site slope, is used in Figure 11b because the spatial variations of depth and velocity are in turn affected by the distribution of the domain slope. Theoretically, the domain slope and contributing area are the dominant factors affecting spatial estimation of flow variables in conditions when runoff production is spatially uniform in the basin. However, the effect of contributing area was not found to be significant in estimating the illustrated morphological changes: a relationship between the elevation changes and the topographic index exhibits a trend similar to that in Figure 11b (not shown). Both plots in Figure 11 reflect similar type of erosion dependence on a prognostic variable: erosion is higher for larger slopes that result in higher velocities and smaller depths, regardless of the magnitude of contributing area. This indicates that this zeroth-order headwater basin had not developed a fluvial convergence region, where erosion scaling with upstream contributing area decreases with

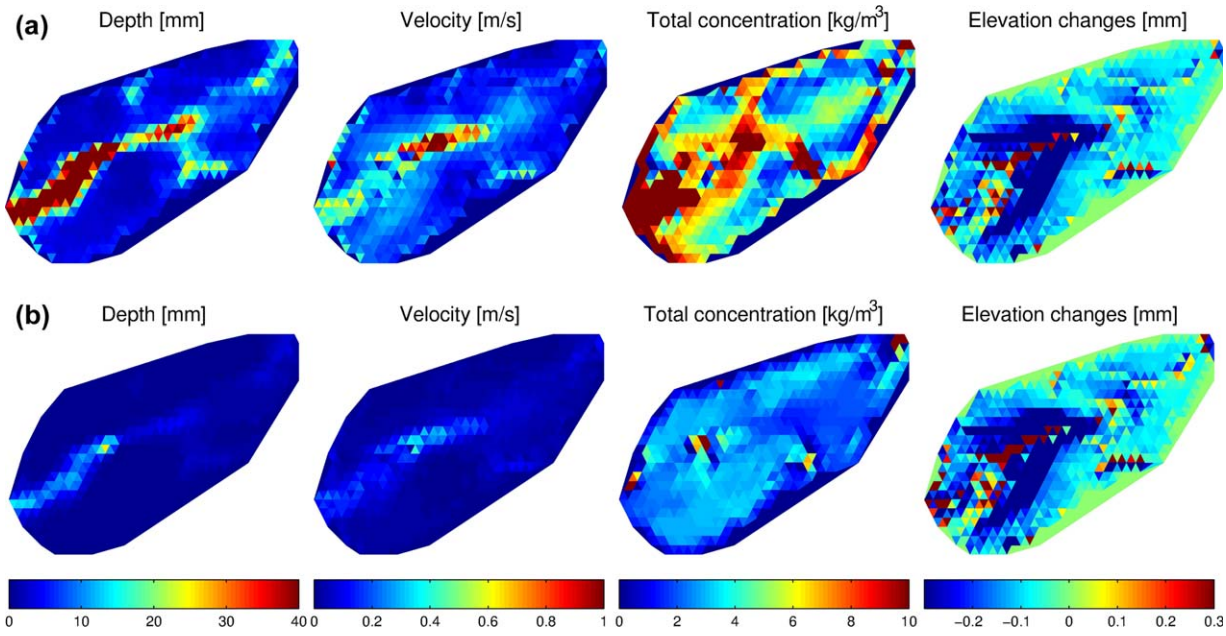

Figure 10. The simulated spatial distributions of depth, velocity, total concentration, and elevation changes at simulation hours (the top set of plots) 1 and (the bottom set of plots) 2 for event 7. In the plots of elevation changes, deposition is represented as positive values and erosion is illustrated with negative values.

the slope. Thus, the overall, basin-scale erosion pattern is that of a "diffusive" mechanism, rather of the fluvial type [*Istanbulluoglu et al.*, 2008; *Francipane et al.*, 2012]. As seen in Figure 11b, erosion dependence on site slope exhibits a threshold (~0.09 for slope) beyond which the elevation changes grow significantly in a nonlinear fashion. This behavior explains the substantial changes of elevation observed in Figure 10 in the area of steep slopes. This result indicates that topographic bed slope can be one of the most dominant factors in determining erosion process in this watershed. Conversely, deposition is more likely to occur as the ratio of flow velocity to depth (or site slope magnitude) decreases. But any generalization is difficult because deposition does not occur frequently in this basin (~8% of the domain).

4.3.4. Size-Dependent Characteristics and Spatial Variability of Concentration

[53] Further investigation of the results presented above is warranted. The simulation results that can explain how the spatial distributions of erosion variables differ depending on sediment particle size are addressed for simulation hour 1 for event 7. First, we confirm that similar to the described verification cases in section 4.1, size-selective characteristics of erosion variables distinctly follow theoretical patterns implied by the H-R equations: the size-selective features in the spatial patterns for e_i and r_i are mainly determined by the ratio of particles (p_i) in the intact soil; the size-selective, spatial patterns for e_{ri} and r_{ri} mostly follow the distribution of M_i (not shown). However, the relative fractions of particle size-specific deposition rate are different from the relative fractions of concentration, i.e., the proportion of the total deposition for larger particles is much higher than that of concentration (not shown). This is because when computing the deposited rate from equation (12), the effect of settling velocity is 1–2 orders of magnitude greater than that of concentration. Second, the region with an abrupt transition from steep to mild slopes is more pronounced in the spatial distributions for coarser sizes

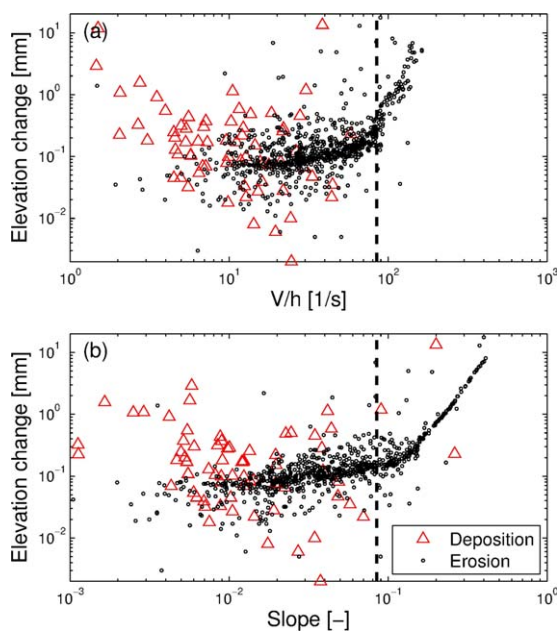

Figure 11. Changes in elevation over the first hour of simulation (event 7) as a function of (a) the ratio of local flow velocity to depth and (b) site bed slope. Red triangles correspond to deposition and black dots correspond to erosion (shown as absolute elevation changes). The vertical dashed line depicts a threshold slope value of 8.47%.

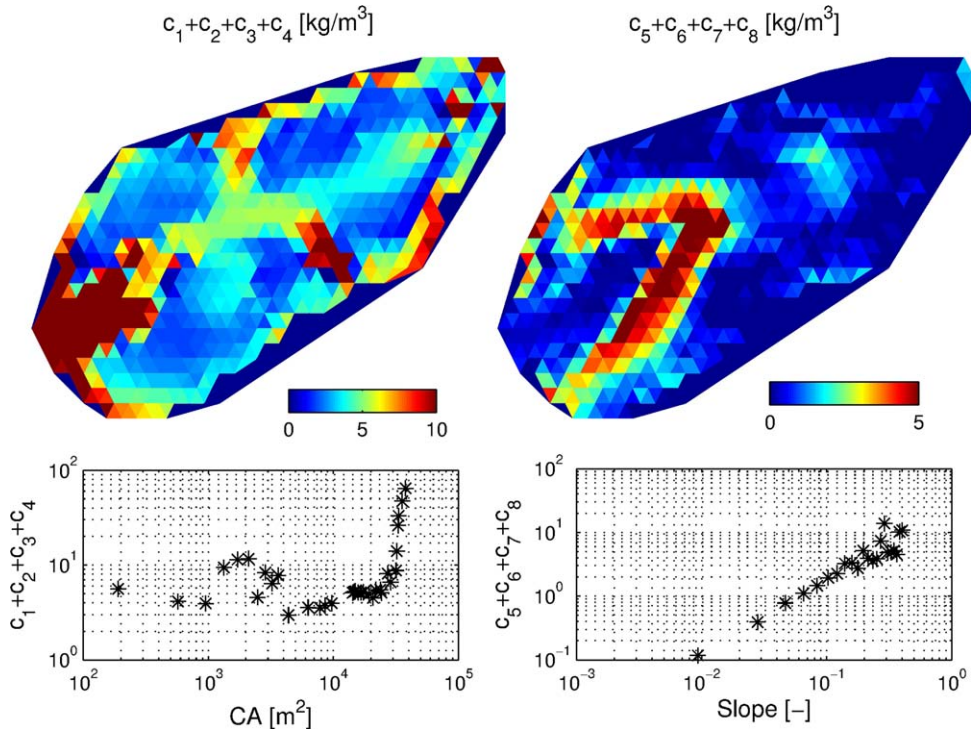

Figure 12. The simulated spatial distributions of the total concentration (in kg/m^3) for (a) smaller particles ($i = 1$, 2, 3, and 4) and (b) larger particles ($i = 5$, 6, 7, and 8) at simulation hour 1 (event 7). Their dependences on contributing area and domain slope are shown in the two bottom plots. The contributing area and slope are binned into 100 intervals; the averaged values for each bin are used in the plots.

(e.g., reentrainment rates for sand and gravel); this may in turn influence the spatial variation of concentrations. Since the former phenomenon is directly anticipated from the H-R equations, we focus on the latter in the following analysis.

[54] The particle size-dependent concentrations of sediment in water column are compared in Figure 12. It shows two distinct patterns of spatial variation and their dependence on contributing area and slope either for smaller particles (clay and silt size) or larger particles (sand and gravel size). This figure illustrates that smaller particles that are easily entrained can move far from their original locations without settling, and thus their concentrations in water flow rapidly increases with contributing area, exhibiting a threshold (~75% of the total CA). In contrast, larger particles are more sensitive to changes in flow conditions and their concentration can abruptly drop due to deposition, should the stream power in combination with topographic slope become too low.

[55] These results imply that as compared to single-sediment-size, supply-transport capacity based formulations of erosion and sediment transport [*Istanbulluoglu et al.*, 2008; *Francipane et al.*, 2012], modeling dynamics of individual sediment sizes can lead to distinctly different, size-specific dependencies on two-dimensional variations in flow and morphologic characteristics. Specifically, unlike the simulated "diffusive" patterns of the total erosion (section 4.3.3) and concentration for larger particles (Figure 12, right), the spatial variations of concentration for smaller particles follow a pattern that is characteristic of "fluvial" erosion, which is determined by the flow rate. Overall, such inferences re-enforce the notion that topographic characteristics of watershed exert a crucial role on soil erosion and sediment transport processes.

4.3.5. Vegetation-Mediated Impacts on Erosion of Hillslope Aspect

[56] Two critical features of watershed systems are their connectivity (i.e., a hydrologically mediated transfer of mass, momentum, energy, or organisms within or between basin compartments [*Michaelides and Chappell*, 2009]), and nonlinearity (i.e., their dynamics depend on "convective" and "dissipative" characteristics of involved processes [*Leopold and Langbein*, 1962; *Zehe and Sivapalan*, 2009]). A case study illustrating how the two features are related through a physical interaction among hydrologic processes, flow regime, erosion, and stream sedimentation is developed in the following. It investigates how disturbances arising at the scale of ecohydrological features of the watershed propagate downstream.

[57] Specifically, we used the spatial distribution of mean annual biomass in the Lucky Hills watershed obtained from earlier simulations reported in [*Istanbulluoglu et al.*, 2008; *Francipane et al.*, 2012]. Figure 13a shows the effect of slope aspect on vegetation distribution: north facing slopes exhibit higher vegetation biomass than south facing elements, a landscape feature of semiarid systems observed and reported in numerous empirical studies [*Gutiérrez-Jurado et al.*, 2007]. We consider two hypotheses of hydrologic and hydraulic behaviors that (i) the larger biomass of north facing slopes implies less runoff production due to higher soil conductivity [*Wainwright et al.*, 2000; *Wilcox et al.*, 2003; *Caldwell et al.*, 2012], and (ii)

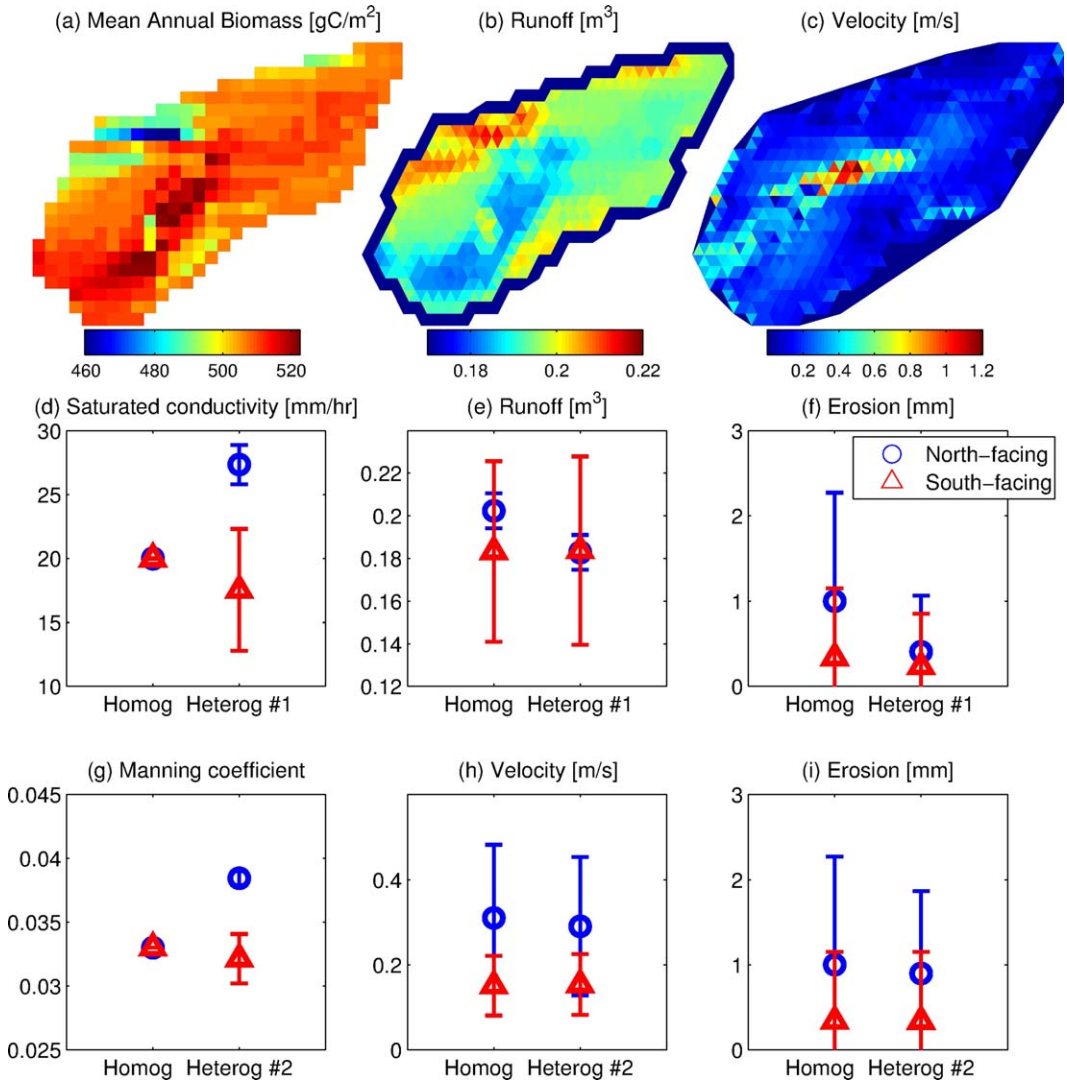

Figure 13. The spatial distribution of (a) mean annual above-ground biomass [*Francipane et al.*, 2012]; (b) simulated total runoff; and (c) velocity at the simulation hour 1 for Event 7. The subplots (d) and (g) represent differences of spatially averaged conductivity and Manning coefficient (introduced based on the magnitude of mean annual biomass, section 4.3.5) between north facing and south facing elements. The subplots (e) and (h) show the differences for simulated runoff and flow velocity. The subplots (f) and (i) illustrate the spatially averaged erosion (eroded areas only) at hour 1: "Homog" denotes the case with spatially uniform saturated hydraulic conductivity and roughness (Event 7); "Heterog 1" corresponds to the case with heterogeneous conductivity; and "Heterog 2" corresponds to the case with spatially distributed friction coefficient.

that flow is retarded on these slopes, because of larger stem density, (thereby potentially leading to an additional positive "dynamic" effect of biomass on infiltration, which is not addressed here). Two experimental cases are designed: (i) one that exhibits spatially distributed saturated conductivity, ranging from 5 to 30 mm/h, as compared to the spatially homogenous value of $K_s = 20$ mm/h of the control case (chosen to be the simulation with spatially uniform inputs for event 7); (ii) the other case has a spatially distributed Manning coefficient ranging from 0.0265 to 0.0395 (0.033 is used in the control case). As the actual spatial variation of saturated conductivity is not available, it is related to the distribution of mean annual above-ground biomass (Figure 13a) such that generated runoff for north facing and south facing hillslopes corresponds to differences of 20–25%, a magnitude obtained in empirical observations by *Gutiérrez-Jurado et al*. [2007]. The distribution of roughness coefficient is estimated from the vegetation cover fraction related to the mean annual biomass using equation (11) in *Kim et al*. [2012a].

[58] The simulation results of the two cases are illustrated in Figures 13b and 13c showing that both runoff and flow velocity in unchannelized areas are inversely related to the biomass distribution, resulting in the decrease of both variables for north facing sites. These can be verified quantitatively by comparing the spatially averaged runoff and flow velocity for all south facing and north facing elements (Figures 13e and 13h). Further, the total erosion in

north facing areas with higher vegetation biomass is smaller, as compared to the control case, because of smaller runoff and velocity (Figures 13f and 13i). Erosion at south facing sites however exhibits little change for both cases of introduced spatial heterogeneity.

[59] The two simulations illustrate how the processes of hydrology, flow hydraulics, and erosion interact with and depend on spatial variations of watershed geometry, soil, and vegetation. The goal is to demonstrate how the integrated modeling system can incorporate a more realistic description of physical complexity perceived to be vital for representing the relevant processes. An emerging feature is basin nonlinearity arising from individual processes and their interactions. For example, ~36% increase of mean saturated conductivity in north facing areas results in ~10 and 60% reductions of runoff and erosion. Approximately 16% increase of Manning coefficient for the same areas leads to ~6 and 10% decreases of velocity and erosion. Further, despite the approximate nature of introduced spatial variations, their emphasis on two "preselected" characteristics, and a lack of uncertainty analysis, the results are arguably the first attempt to describe mechanistically the coupled dynamics that are likely to underlie broad patterns of landscape geometry observed over large areas of the western United States. [*Poulos et al.*, 2012].

5. Summary

[60] A novel two-dimensional, physically based model of soil erosion and sediment transport has been developed and coupled to a model that can simulate both hydrodynamic flow motions and hydrologic surface and subsurface processes. The erosion and transport processes are described with the Hairsine-Rose (H-R) model that accounts for size-selective sediment transport, differentiates soil of the bed into original and deposited soil layers, and tracks in time the development of the deposited area. The hydrologic and hydrodynamic model is tRIBS-OFM, Triangulated irregular network-based, Real time Integrated Basin Simulator-Overland Flow Model. For the solution of the combined two-dimensional, Saint-Venant and Hairsine-Rose equations, the finite volume method is employed, based on Roe's approximate Riemann solver. The domain is resolved on an unstructured, multiple resolution triangular mesh. The equations yielding space-time dynamics of flow, erosion, and sediment transport thus represent a coupled system of shallow water equations combined with advection-dominated transport equations for sediment of multiple particle sizes.

[61] The integrated model has been verified with analytical solutions and empirical data for two one-dimensional benchmark cases describing rainfall- and overland flow-induced erosion. The size-selective results of spatial distributions of sediment concentrations and deposited masses at different times, as well as temporal distributions, are presented and demonstrate a good agreement with measured data.

[62] The model has been consequently applied at the catchment scale, to the Lucky Hills watershed located in southeastern Arizona, USA. Sensitivity tests to the number of particle sizes representing soil texture and to the mesh resolution describing domain geometry were performed. Model confirmation was carried out for both flow volume and sediment yield at the basin outlet for 10 rainfall events. As the simulation results indicate, an overall "diffusion-like" type of erosion is characteristic of this headwater, zeroth-order catchment: erosion increases with slope and is not greatly affected by the contributing area. In particular, large elevation changes due to erosion occur over a limited hillslope area with abrupt morphological changes: for slopes higher than a particular threshold, erosion grows significantly and in a nonlinear fashion. When sediment concentration in surface flow is partitioned according to particle sizes, the spatial distributions exhibit two types of dependencies: with site slope, for larger particles, and with contributing area, for smaller particles. The results emphasize the importance of different basin topographic characteristics in determining the amount of sediment in water column, as mediated by the dynamic flow regime of depth and velocity.

[63] Lastly, additional physical complexity was introduced in simulations by changing the spatial distribution of surface and subsurface conditions of the Lucky Hills watershed according to empirically observed dependencies on distribution of vegetation biomass. Two simulations elucidate how the processes of hydrology, flow hydraulics, and erosion are affected by spatial heterogeneity of soil and surface roughness conditions. The results illustrate that north facing and south facing slopes can have different responses to the same hydrologic events; further efforts are needed to mechanistically address hierarchy of processes underlying the formation of patterns of hillslope geometry observed over large areas of arid and semiarid climate.

[64] This study builds on and expands previous research by using a coupled framework that adapts the erosion and sediment transport model to watershed-scale simulations. The essential strengths of the combined framework are as follows. (1) Hydrologic and hydraulic characteristics as well as particle size distribution, arguably the three most crucial elements among external and internal factors for modeling erosion, are all simultaneously taken into consideration at the application scale of a watershed. (2) The model is based on sound physical laws, which results in narrow ranges of parameter values that are theoretically measurable; satisfactory results can thus be obtained with minimum calibration efforts. This model attribute makes feasible a wider range of real-world, catchment-scale flow/erosion problems. (3) The spatially distributed, detailed information on soil type, land use, and topography is becoming more accurate and easily accessible. This generates the potential for making modeling of earth-surface processes more credible. By incorporating these types of information, the developed hydrologic-hydrodynamic-erosion coupled model can be used as an assessment tool for quantitative evaluation of spatiotemporal erosion responses to imposed scenarios of climate change, variations in land-use, soil, and vegetation types in small- to medium-size basins.

Notation

Parameter	Description
A	Area of triangular cell.
a	Celerity.
a_0	Detachability of original soil.
a_d	Detachability of deposited soil.

b Exponent used in equation (9).
C_D Bed drag coefficient.
C_r Courant number.
c_i Sediment concentration.
$\mathbf{D}$ Erosion rates vector.
D_R Mean raindrop size.
D_{50} Median particle size.
d_i Deposition rate.
$\mathbf{E}$ x-Directional flux vector.
e_i Rainfall driven detachment rate.
e_{ri} Rainfall driven redetachment rate.
$\mathbf{F}$ Flux vector.
F Effective fraction of excess stream power.
F_w Shield effect factor.
$\mathbf{G}$ y-Directional flux vector.
g Acceleration constant due to gravity.
H Shielding proportion.
h Flow depth.
h_0 Threshold used in equation (9).
I The number of sediment size classes.
i Particle size class.
J Specific energy of entrainment.
j Cell index.
k Face index.
L Left side of the cell interface.
$\hat{L}$ Left eigenvector.
l Length of triangular edge.
$\mathbf{M}$ Sediment mass vector.
M_i Deposited mass of each sediment size.
M_t Total deposited mass.
M_t^* Deposited mass needed to sheild original soil.
m A fuction that has 1 or -1 depending on whether the unit vector directs outward of inward.
N_c The number of triangular cells.
$\mathbf{n}$ Outward-directed unit vector normal to the boundary.
n Manning coefficient.
P Precipitation intensity.
p_i Ratio of sediment class i.
R Right side of the cell interface.
$\hat{R}$ Right eigenvector.
r_i Flow induced entrainment rate.
r_{ri} Flow induced reentrainment rate.
$\mathbf{S}$ Source vector.
S Domain slope.
S_{fx} X-directional friction slope.
S_{fy} Y-directional friction slope.
S_r Net runoff production rate.
$\mathbf{U}$ Conservative variable vector.
u X-directional velocity.
v Y-directional velocity.
z_b Bed elevation at cell center.
Γ Boundary of the control volume.
$\hat{\Lambda}$ Eigenvalue.
Ω Stream power.
Ω_{cr} Critical stream power.
Ω_x x-Directional stream power.
Ω_y y-Directional stream power.
$\emptyset$ Angle between the face normal vector and the x axis.
β Porosity of bed.
θ_c Critical Shields parameter for incipient motion.
ν_i Settling velocity.
ν_R Rainfall impact velocity.
ρ_s Density of sediment.
ρ_w Density of water.
λ Eigenvalue.
Δ Finite difference across the interface.
$\Delta\hat{V}$ Wave strength.

[65] **Acknowledgments.** This work was supported by NSF grant EAR 1151443 "CAREER: A Multiscale Approach to Assessment of Climate Change Impacts on Hydrologic and Geomorphic Response of Watershed Systems within an Uncertainty Framework."

References

Abbott, M. B. (1974), Continuous flows, discontinuous flows and numerical analysis, *J. Hydraul. Res.*, *12*(4), 417–467.

Aksoy, H., and M. L. Kavvas (2005), A review of hillslope and watershed scale erosion and sediment transport models, *Catena*, *64*(2-3), 247–271.

Bagnold, R. A. (1966), An approach to the sediment transport problem for general physics, *U.S. Geol. Surv. Prof. Pap.*, *442-I*, p. I1–I37, USGS, Washington, D. C.

Bai, Z. G., D. L. Dent, L. Olsson, and M. E. Schaepman (2008), Proxy global assessment of land degradation, *Soil Use Manage.*, *24*, 223–234.

Begnudelli, L., and B. F. Sanders (2006), Unstructured grid finite-volume algorithm for shallow-water flow and scalar transport with wetting and drying, *J. Hydraul. Eng.*, *132*(4), 371–384.

Begnudelli, L., and B. F. Sanders (2007), Simulation of the St. Francis dam-break flood, *J. Eng. Mech.*, *133*, 1200–1212.

Beuselinck, L., G. Govers, A. Steegen, and P. B. Hairsine (1998), Experiments on sediment deposition by overland flow, *Modell. Soil Erosion, Sediment Transp. Closely Related Hydrol. Processes*, (249), 91–96.

Beuselinck, L., G. Govers, A. Steegen, and T. A. Quine (1999), Sediment transport by overland flow over an area of net deposition, *Hydrol. Processes*, *13*(17), 2769–2782.

Begnudelli, L., B. F. Sanders, and S. F. Bradford (2008), Adaptive Godunov-based model for flood simulation, *J. Hydraul. Eng.*, *134*(6), 714–725.

Bradford, S. F., and N. D. Katopodes (1999), Hydrodynamics of turbid underflows, I: Formulation and numerical analysis, *J. Hydraul. Eng.*, *125*(10), 1006–1015.

Bradford, S. F., and N. D. Katopodes (2001), Finite volume model for nonlevel basin irrigation, *J. Irrig. Drain. Eng.*, *127*(4), 216–223.

Bradford, S. F., and B. F. Sanders (2002), Finite-volume model for shallow-water flooding of arbitrary topography, *J. Hydraul. Eng.*, *128*(3), 289–298.

Brown, L. R. (1984), *Conserving soils, in State of the World*, edited by L. R. Brown, pp. 53–75, Norton, New York.

Brufau, P., and P. Garcia-Navarro(2003), Unsteady free surface flow simulation over complex topography with a multidimensional upwind technique, *J. Comput. Phys.*, *186*(2), 503–526.

Brufau, P., P. Garcia-Navarro, and M. E. Vazquez-Cendon(2004), Zero mass error using unsteady wetting-drying conditions in shallow flows over dry irregular topography, *Int. J. Numer. Methods Fluids*, *45*(10), 1047–1082.

Bunn, S. E., and A. H. Arthington (2002), Basic principles and ecological consequences of altered flow regimes for aquatic biodiversity, *Environ. Manage.*, *30*(4), 492–507.

Buringh, P. (1981), *An assessment of losses and degradation of productive agricultural land in the world, Working Group on Soils Policy*, Food Agricultural Organization, Rome.

Cabral M. C., L. Garrote, R. L. Bras, and D. Entekhabi (1992), A kinematic model of infiltration and runoff generation in layered and sloped soils, *Adv. Water Resour.*, *15*, 311–324.

Caldwell, T. G., M. H. Young, E. V. McDonald, and J. Zhu (2012), Soil heterogeneity in Mojave Desert shrublands: Biotic and abiotic processes, *Water Resour. Res.*, *48*, W09551, doi:10.1029/2012WR011963.

Cao, Z., R. Day, and S. Egashira (2002), Coupled and decoupled numerical modeling of flow and morphological evolution in alluvial rivers, *J. Hydraul. Eng.*, *128*(3), 306–321.

Cao, Z., G. Pender, S. Wallis, and P. Carling (2004), Computational dam-break hydraulics over erodible sediment bed, *J. Hydraul. Eng.*, *130*(7), 689–703.

Cheng, N. (1997), Simplified settling velocity formula for sediment particle, *J. Hydraul. Eng.*, *123*(2), 149–152.

Deardorff, J. W. (1978), Efficient prediction of ground surface temperature and moisture, with inclusion of a layer of vegetation, *J. Geophys. Res.*, *83*(C4), 1889–1903.

Dunne, T., and R. D. Black (1970), An experimental investigation of runoff production in permeable soils, *Water Resour. Res.*, *6*(2), 478–490.

Eltahir, E. A. B., and R. L. Bras (1993), A description of rainfall interception over large areas, *J. Clim.*, *6*, 1002–1008.

Entekhabi, D. (2000), Land Surface Processes: Basic Tools and Concepts, Department of Civil and Environmental Engineering, MIT, Cambridge, Mass.

Fiener, P., G. Govers, and K. Van Oost (2008), Evaluation of a dynamic multi-class sediment transport model in a catchment under soil-conservation agriculture, *Earth Surf. Processes Landforms*, *33*(11), 1639–1660.

Francipane, A., V. Y. Ivanov, L. V. Noto, E. Istanbulluoglu, E. Arnone, and R. L. Bras (2012), tRIBS-Erosion: A parsimonious physically-based model for studying catchment hydro-geomorphic response, *Catena*, *92*, 216–231.

Goodrich, D. C., T. O. Keefer, C. L. Unkrich, M. H. Nichols, H. B. Osborn, J. J. Stone, and J. R. Smith (2008), Long-term precipitation database, Walnut Gulch Experimental Watershed, Arizona, United States, *Water Resour. Res.*, *44*, W05S04, doi:10.1029/2006WR005782.

Gutiérrez-Jurado, H. A., E. R. Vivoni, E. Istanbulluoglu, and R. L. Bras (2007), Ecohydrological response to a geomorphically significant flood event in a semiarid catchment with contrasting ecosystems, *Geophys. Res. Lett.*, *34*, L24S25, doi:10.1029/2007GL030994.

Hairsine, P. B., and C. W. Rose (1991), Rainfall detachment and deposition: Sediment transport in the absence of flow-driven processes, *Soil Sci. Soc. Am. J.*, *55*(2), 320–324.

Hairsine, P. B., and C. W. Rose (1992), Modeling water erosion due to overland flow using physical principles: 1. Sheet flow, *Water Resour. Res.*, *28*(1), 237–243.

Hairsine, P. B., G. C. Sander, C. W. Rose, J. Y. Parlange, W. L. Hogarth, I. Lisle, and H. Rouhipour (1999), Unsteady soil erosion due to rainfall impact: A model of sediment sorting on the hillslope, *J. Hydrol.*, *220*(3-4), 115–128.

Heng, B. C. P., G. C. Sander, and C. F. Scott (2009), Modeling overland flow and soil erosion on nonuniform hillslopes: A finite volume scheme, *Water Resour. Res.*, *45*, W05423, doi:10.1029/2008WR007502.

Heng, B. C. P., G. C. Sander, A. Armstrong, J. N. Quinton, J. H. Chandler, and C. F. Scott (2011), Modeling the dynamics of soil erosion and size-selective sediment transport over nonuniform topography in flume-scale experiments, *Water Resour. Res.*, *47*, W02513, doi:10.1029/2010WR009375.

Hirsch, C. (1990), *Numerical Computation of Internal and External Flows*, John Wiley, New York.

Hogarth, W. L., C. W. Rose, J. Y. Parlange, G. C. Sander, and G. Carey (2004a), Soil erosion due to rainfall impact with no inflow: A numerical solution with spatial and temporal effects of sediment settling velocity characteristics, *J. Hydrol.*, *294*(4), 229–240.

Hogarth, W. L., J. Y. Parlange, C. W. Rose, G. C. Sander, T. S. Steenhuis, and A. Barry (2004b), Soil erosion due to rainfall impact with inflow: An analytical solution with spatial and temporal effects, *J. Hydrol.*, *295*(1-4), 140–148.

Horton, R. E. (1933), The role of infiltration in the hydrological cycle, *Trans., Am. Geophys. Union*, *14*, 446–460.

Hu, Z., and S. Islam (1995), Prediction of ground surface temperature and soil moisture content by the force-restore method, *Water Resour. Res.*, *31*(10), 2531–2539.

Huang, C., L. K. Wells, and L. D. Norton (1999), Sediment transport capacity and erosion processes: Model concepts and reality, *Earth Surf. Processes Landforms*, *24*(6), 503–516.

Hursh, C. R., and E. F. Brater (1941), Separating storm-hydrographs from small drainage-areas into surface and subsurface flow, *Trans., Am. Geophys. Union*, *22*, 863–870.

Istanbulluoglu, E., O. Yetemen, E. R. Vivoni, H. A. Gutierrez-Jurado, and R. L. Bras (2008), Eco-geomorphic implications of hillslope aspect: Inferences from analysis of landscape morphology in central New Mexico, *Geophys. Res. Lett.*, *35*, L14403, doi:10.1029/2008GL034477.

Ivanov, V. Y., E. R. Vivoni, R. L. Bras, and D. Entekhabi (2004a), Preserving high-resolution surface and rainfall data in operational-scale basin hydrology: A fully-distributed physically-based approach, *J. Hydrol.*, *298*(1-4), 80–111.

Ivanov, V. Y., E. R. Vivoni, R. L. Bras, and D. Entekhabi (2004b), Catchment hydrologic response with a fully distributed triangulated irregular network model, *Water Resour. Res.*, *40*, W11102, doi:10.1029/2004WR003218.

Kim, J., V. Y. Ivanov, and N. D. Katopodes (2012a), Hydraulic resistance to overland flow on surfaces with partially submerged vegetation, *Water Resour. Res.*, *48*, W10540, doi:10510.11029/12012WR012047.

Kim, J., A. Warnock, V. Y. Ivanov, and N. D. Katopodes (2012b), Coupled modeling of hydrologic and hydrodynamic processes including overland and channel flow, *Adv. Water Resour.*, *37*, 104–126.

Laws, J. O., and D. A. Parsons (1943), The relation of raindrop size to intensity, *Trans. Am. Geophys. Union*, *24*, 452–460.

Leendertse, J. J. (1967), Aspects of a computational model for long-period water wave propagation, *Memor. RM-5294-PR*, The Rand Corp., Santa Monica, Calif.

Leopold, L. B., and W. L. Langbein (1962), The concept of entropy in landscape evolution, *U.S. Geol. Surv. Prof. Pap.*, *500-A*, p. A1–A20, USGS, Washington, D. C.

Liggett, J. A. (1968), Mathematical flow determination in open channels, *J. Eng. Mech. Div.*, *94*(EM4), 947–963.

Lin, J. D. (1980), On the force-restore method for prediction of ground surface temperature, *J. Geophys. Res.*, *85*(C6), 3251–3254.

Merritt, W. S., R. A. Letcher, and A. J. Jakeman (2003), A review of erosion and sediment transport models, *Environ. Modell. Software*, *18*(8-9), 761–799.

Michaelides, K., and A. Chappell (2009), Connectivity as a concept for characterising hydrological behaviour, *Hydrol. Processes*, *23*, 517–522.

Monteith, J. L. (1965), Evaporation and environment, *Symposia of the Society for Experimental Biology*, *19*, 205–234.

Murillo, J., P. Garcia-Navarro, P. Brufau, and J. Burguete (2008), 2D modelling of erosion/deposition processes with suspended load using upwind finite volumes, *J. Hydraul. Res.*, *46*(1), 99–112.

Mutchler, C. K., and K. C. McGregor (1983), Erosion from low slopes, *Water Resour. Res.*, *19*(5), 1323–1326.

Nearing, M. A., M. H. Nichols, J. J. Stone, K. G. Renard, and J. R. Simanton (2007), Sediment yields from unit-source semiarid watersheds at Walnut Gulch, *Water Resour. Res.*, *43*, W06426, doi:10.1029/2006WR005692.

Nichols, M. H., J. J. Stone, and M. A. Nearing (2008), Sediment database, Walnut Gulch Experimental Watershed, Arizona, United States, *Water Resour. Res.*, *44*, W05S06, doi:10.1029/2006WR005682.

Noel, D. U. (2001), A note on soil erosion and its environmental consequences in the United States, *Water Air Soil Pollut.*, *129*(1), 181–197.

Nord, G., and M. Esteves (2005), PSEM_2D: A physically based model of erosion processes at the plot scale, *Water Resour. Res.*, *41,W08407*, doi:10.1029/2004WR003690.

Noto, L. V., V. Y. Ivanov, R. L. Bras, and E. R. Vivoni (2008), Effects of initialization on response of a fully-distributed hydrologic model, *J. Hydrol.*, *352*(1-2), 107–125.

Oldeman, L. R., R. T. A. Hakkeling, and W. G. Sombroek (1991), *World Map of the Status of Human-Induced Soil Degradation*, 2nd ed., Int. Soil Ref. and Inf. Cent., Wageningen.

Papanicolaou, A. N., J. T. Sanford, D. C. Dermisis, and G. A. Mancilla (2010), A 1-D morphodynamic model for rill erosion, *Water Resour. Res.*, *46*, W09541, doi:10.1029/2009WR008486.

Parlange, J. Y., W. L. Hogarth, C. W. Rose, G. C. Sander, P. Hairsine, and I. Lisle (1999), Addendum to unsteady soil erosion model, *J. Hydrol.*, *217*(1-2), 149–156.

Penman, H. L. (1948), Natural evaporation from open water, bare soil and grass, *Proc. R. Soc. London, Ser. A.*, *A193*, 120–145.

Pimentel, D., et al. (1995), Environmental and economic costs of soil erosion and conservation benefits, *Science*, *267*(5201), 1117–1123.

Poff, N. L., and J. D. Allan (1995), Functional organization of stream fish assemblages in relation to hydrological variability, *Ecology*, *76*(2), 606–627.

Poff, N. L., and J. K. H. Zimmerman (2010), Ecological responses to altered flow regimes: A literature review to inform the science and management of environmental flows, *Freshwater Biol.*, *55*(1), 194–205.

Poulos, M. J., J. L. Pierce, A. N. Flores, and S. G. Benner (2012), Hillslope asymmetry maps reveal widespread, multi-scale organization, *Geophys. Res. Lett.*, *39*, L06406, doi:10.1029/2012GL051283.

Proffitt, A. P. B., C. W. Rose, and P. B. Hairsine (1991), Rainfall detachment and deposition: Experiments with low slopes and significant water depths, *Soil Sci. Soc. Am. J.*, *55*(2), 325–332.

Renard, K. G., J. R. Simanton, and C. E. Fancher (1986), Small watershed automatic water quality sampler, edited, in Proceedings of the 4th Federal Interagency Sedimentation Conference, Las Vegas, Nev., pp. 1–51 to 51–58, United States Government Printing Office, Washington, D. C.

Rinehart A. J., E. R. Vivoni, and P. D. Brooks (2008), Effects of vegetation, albedo, and solar radiation sheltering on the solution of snow in the Walles Caldera, New Mexico, *Ecohydrology 1*, 253–270.

Roe, P. L. (1981), Approximate Riemann solvers, parameter vectors, and difference-schemes, *J. Comput. Phys.*, *43*(2), 357–372.

Rutter, A. J., K. A. Kershaw, P. C. Robins, and A. J. Morton (1971), A predictive model of rainfall interception in forests, 1. Derivation of the model from observation in a plantation of Corsican pine, *Agri. Meteorol.*, *9*, 367–384.

Rutter, A. J., A. J. Morton, and P. C. Robins (1975), A predictive model of interception in forests, 2. Generalization of the model and comparison with observations in some coniferous and hardwood stands., *J. Appl. Ecol.*, *12*, 367–380.

Sander, G. C., P. B. Hairsine, C. W. Rose, D. Cassidy, J. Y. Parlange, W. L. Hogarth, and I. G. Lisle (1996), Unsteady soil erosion model, analytical solutions and comparison with experimental results, *J. Hydrol.*, *178*(1-4), 351–367.

Sander, G. C., P. B. Hairsine, L. Beuselinck, and G. Govers (2002), Steady state sediment transport through an area of net deposition: Multisize class solutions, *Water Resour. Res.*, *38*(6), doi:10.1029/2001WR000323.

Sander, G. C., T. Zheng, and C. W. Rose (2007), Update to ''Modeling water erosion due to overland flow using physical principles: 1. Sheet flow'', *Water Resour. Res.*, *43*, W04408, doi:10.1029/2006WR005601.

Sanders, B. F. (2008), Integration of a shallow water model with a local time step, *J. Hydraul. Res.*, *46*(4), 466–475.

Sanders, B. F., J. E. Schubert, and H. A. Gallegos (2008), Integral formulation of shallow-water equations with anisotropic porosity for urban flood modeling, *J. Hydrol.*, *362*(1-2), 19–38.

Simpson, G., and S. Castelltort (2006), Coupled model of surface water flow, sediment transport and morphological evolution, *Comput. Geosci.*, *32*(10), 1600–1614.

Stone, J. J., M. H. Nichols, D. C. Goodrich, and J. Buono (2008), Long-term runoff database, Walnut Gulch Experimental Watershed, Arizona, United States, *Water Resour. Res.*, *44*, W05S05, doi:10.1029/2006WR005733.

Titov, V. V., and C. E. Synolakis (1995), Modeling of breaking, and non-breaking long-wave evolution and runup using VTCS-2, *J. Waterway Port Coastal Ocean Eng.*, *121*(6), 308–316.

Tromp-van Meerveld, H. J., J. Y. Parlange, D. A. Barry, M. F. Tromp, G. C. Sander, M. T. Walter, and M. B. Parlange (2008), Influence of sediment settling velocity on mechanistic soil erosion modeling, *Water Resour. Res.*, *44*, W06401, doi:10.1029/2007WR006361.

Wainwright, J., A. J. Parsons, and A. D. Abrahams (2000), Plot-scale studies of vegetation, overland flow and erosion interactions: Case studies from Arizona and New Mexico, *Hydrol. Processes*, *14*, 2921–2943.

Weyman, D. R. (1970), Throughflow on hillslopes and its relation to the stream hydrograph, *Hydrol. Sci. Bull.*, *15*, 25–33.

Wilcox, B. P., D. D. Breshears, and H. J. Turin (2003), Hydraulic conductivity in a Piñon-Juniper Woodland: Influence of vegetation, *Soil Sci. Soc. Am. J.*, *67*, 1243–1249.

Xia, J., R. A. Falconer, B. Lin, and T. G. (2010), Modelling flood routing on initially dry beds with refined treatment of wetting and drying, *Int. J. River Basin Manage.*, *8*(3-4), 225–243.

Zehe, E., and M. Sivapalan (2009), Threshold behaviour in hydrological systems as (human) geo-ecosystems: manifestations, controls, implications, *Hydrol. Earth Syst. Sci.*, *13*(7), 1273–1297.